International Journal of Plasticity 105 (2018) 141–163

Contents lists available at ScienceDirect

International Journal of Plasticity

journal homepage: www.elsevier.com/locate/ijplas

Latent hardening within the elasto-plastic self-consistent polycrystal homogenization to enable the prediction of anisotropy of AA6022-T4 sheets

Milovan Zecevic, Marko Knezevic*

Department of Mechanical Engineering, University of New Hampshire, Durham, NH 03824, USA

ARTICLE INFO

Keywords:
Microstructures
Crystal plasticity
Polycrystalline material
Numerical algorithms
AA6022-T4

ABSTRACT

Slip system hardening behavior of a given slip system is influenced more by shearing on another slip system known, as latent hardening, than by shearing on itself, known as self-hardening. This paper extends a recently developed dislocation-based hardening law within the elasto-plastic self-consistent polycrystal plasticity model to incorporate the latent hardening effects for predicting anisotropic response of polycrystalline face-centered cubic metals. In doing so, a new approach to overcome singularities associated with the self-consistent Eshelby solution procedure is proposed. The new approach is validated using a regularized Schmid law, where the singularity in Eshelby tensor calculation is intrinsically suppressed. Moreover, the solution procedure for single crystal stress increment is advanced to be based on a methodology involving the singular value decomposition to solve for shear increments. It is found that modeling crystallographic texture evolution and latent hardening successfully captures the anisotropic behavior of polycrystalline AA6022-T4 alloy. The model is subsequently successfully applied to predict large strain cyclic deformation of the same material. The implementation and insights from these predictions are presented and discussed in this paper.

1. Introduction

Anisotropy in flow stress of Al and Al alloys has been thoroughly studied, and several possible sources of anisotropy have been identified in the literature, including an initial texture and texture evolution, precipitate shape and orientation, dislocation cell structure formation, and latent hardening. Experimental observations suggested that the anisotropic hardening behavior could result mostly from crystallographic texture evolution. For instance, a study on anisotropy exhibited by commercially pure Al (AA1050-O) suggested that initial texture and texture evolution was the main reason for anisotropy (Lopes et al., 2003).The shape and direction of precipitates was related to plastic anisotropy in Al-Si-Mg alloys (Anjabin et al., 2014) and in Al-Cu alloys (Sehitoglu et al., 2005). These alloys contain precipitates that are larger in size meaning that they are not shearable. Therefore, their effect was analyzed by assuming that they are inclusions inside the matrix (Lyttle and Wert, 1999). The backstress in matrix was defined based on the stress in the precipitates, since the volume average of backstress over matrix and precipitates vanishes. However, the effect of precipitates on anisotropy in the AA6022-T4 is not expected to be high because these precipitates are small in size and shearable by mobile dislocations. Studies on pure Al (Juul Jensen and Hansen, 1990) as well as on the alloys with very small shearable precipitates showed that texture alone is not enough to explain the anisotropy. Predictions based on texture sensitive crystal plasticity models

---

* Corresponding author. Department of Mechanical Engineering, University of New Hampshire, 33 Academic Way, Kingsbury Hall, W119, Durham, NH 03824, USA.
E-mail address: marko.knezevic@unh.edu (M. Knezevic).

https://doi.org/10.1016/j.ijplas.2018.02.007
Received 22 September 2017; Received in revised form 30 January 2018; Accepted 10 February 2018

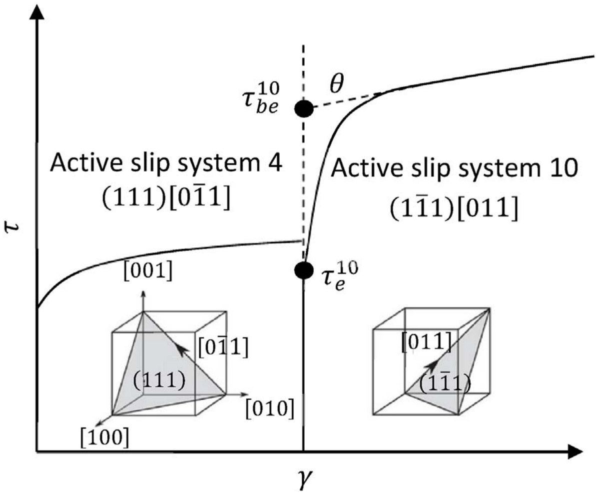

Fig. 1. Schematic showing hardening of the secondary slip system $s = 10$ due to shearing on the primary slip system $s = 4$ according to the elastic limit theory of yielding τ_{e}^{10} and the back-extrapolated theory of yielding τ_{be}^{10}. Shear strain and resolved shear stress are plotted on the x-axis and the y-axis, respectively. The slip systems are labeled according to commonly used notation for FCC metals from (Schmid and Boas, 1950).

often over predict hardening anisotropy compared to experimental measurements (Zhang et al., 2015). Another study revealed that the formation of dislocation cell structures was a major source of anisotropic hardening in AA1050-O, particularly during strain path change deformation (Rauch et al., 2002). While AA1050-O was found to develop a well-defined dislocation microstructure during deformation, predominantly dislocation walls on the {111} planes, the AA6022-T4 alloy develops primarily uniform dislocation distribution displaying some walls, which are very faint (Yoon et al., 2005). Thus, the effect of substructure on anisotropy of AA6022-T4 was suggested to be minimal. The effect of latent hardening and dislocation interactions on plastic anisotropy evolution using crystal plasticity was investigated in (Khadyko et al., 2016), where a solid solution strengthened alloy without precipitates is examined. The general trends were successfully explained by latent hardening.

Slip system hardening behavior of a given slip system is complex because it is influenced more by shearing on another slip system, known as latent hardening, than by shearing on itself, known as self-hardening (Franciosi et al., 1980). Additionally, the slip resistance increases not only on the active but also on the inactive slip systems. The latent hardening was documented first for single crystals in (Taylor and Elam, 1923). The single crystal latent hardening experiments can be conducted as follows: first, a single crystal is deformed to activate a single slip system, termed as the primary slip system. Next, the loading is changed with respect to the initial crystal orientation to activate another slip system, termed as the secondary slip system. The evolution of slip resistances on primary and secondary slip systems can be inferred from the stress strain measurements (Bassani and Wu, 1991b; Franciosi et al., 1980; Kocks and Brown, 1966). Two theories of latent hardening can be found in the literature (Cuitino and Ortiz, 1993). These theories are schematically presented in Fig. 1. Accordingly, yielding of secondary slip system is defined by: the back-extrapolated yield stress (Anand and Kothari, 1996; Franciosi et al., 1980; Peirce et al., 1982) (hereafter referred to as "theory 1") and the elastic limit (Bassani and Wu, 1991a; Cuitino and Ortiz, 1993; Wu et al., 1991a) (hereafter referred to as "theory 2"). The former is obtained by back-extrapolation using the initial hardening slope, θ, of the stress-strain curve recorded during the activation of secondary slip system, to the end of the stress-strain curve of the primary slip system (Kocks and Brown, 1966). Theory 1 view on latent hardening is grossly predominant in the literature and is supported with a large body of studies performed since 1960s, hence it is termed as theory 1, while the more recently proposed theory of Bassani and Wu in 1991a,b is termed as theory 2.

In theory 1 the shear strain on a given slip system leads to an increase in slip resistance of all slip systems, which can be mathematically expressed as:

$$\tau_{be}^{s} = \tau_{be}^{s}(\gamma^1, \gamma^2, ...\gamma^n);\ h^{ss'} = \frac{\partial \tau_{be}^{s}}{\partial \gamma^{s'}} = f(\gamma^1, \gamma^2, ...\gamma^N). \tag{1}$$

where τ_{be}^{s} is the slip resistance based on the back-extrapolated yield stress and the matrix of partial derivatives of slip resistance with respect to shear strain, $\frac{\partial \tau_{be}^{s}}{\partial \gamma^{s'}}$, is hardening matrix. Entries of the hardening matrix are also referred to as the hardening moduli or instantaneous moduli. We note that according to theory 1, hardening matrix is predicted to have off diagonal terms. The added advantage of theory 1 is that it is possible to define a law for the evolution of slip resistance and then derive the corresponding hardening matrix. Therefore, the focus in theory 1 is on slip resistance, while the hardening matrix is defined by partial derivatives with respect to shear strain.

Experimental data presented in (Wu et al., 1991a) formed basis for the development of theory 2 (Bassani and Wu, 1991b). In this theory, the rate of hardening $h^{ss}(\gamma^1, \gamma^2, \gamma^3, ..\gamma^N)$ of a given slip system s depends on shearing on itself $F(\gamma^s)$ and shearing on all the other slip systems $G(\gamma^{s'}; s' = 1..N,\ s' \neq s)$, i.e. the rate of hardening is the product of F and G ($h^{ss} = FG$). However, the slip resistance of a given slip system s increases primarily due to shear strain (activity) on that slip system because the hardening matrix is diagonal or diagonal dominant i.e., $h^{ss} \gg h^{ss'}$. Neglecting the small off-diagonal terms for the case of diagonal dominant hardening matrix, theory 2 can be mathematically expressed as:

$$d\tau_e^s = h^{ss} d\gamma^s;\ \ h^{ss} = f\,(\gamma^1, \gamma^2, \dots\gamma^N);\ \ h^{ss'} = 0 \tag{2}$$

where τ_e^s and γ^s are slip resistance based on the elastic limit, shear strain on *sth* slip system, and N is the total number of slip systems. In Eq. (2), there is no implied summation over repeated indeces. The focus is on the hardening rate. Intrinsic to this theory is that it evolves hardening rate while keeping the slip resistance constant until the activation happens, when the hardening takes place to increase the slip resistance.

The response of a polycrystal depends on the constituent single crystals, whose response is affected by latent hardening. The response of single crystals undergoes homogenization to represent the overall behavior of a polycrystalline metal. Homogenization schemes such as upper bound Taylor-type (Fromm et al., 2009; Knezevic et al., 2008, 2009; Savage and Knezevic, 2015; Shaffer et al., 2010; Taylor, 1938), mean-field self-consistent (SC) (Lebensohn and Tomé, 1993; Lebensohn et al., 2016; Zecevic et al., 2017b), full-field finite element (Ardeljan et al., 2014, 2017; Ardeljan et al., 2015a, 2015b, 2016a, 2016b; Beaudoin et al., 1994; Knezevic et al., 2013b, 2013c; Maudlin and Schiferl, 1996), and Green's function-based fast Fourier transforms (Eghtesad et al., 2017; Lebensohn, 2001) are most widely used. The SC homogenization approach is the most widely used because it provides the best compromise between computational speed and accuracy.

A number of polycrystal plasticity models consider both self and latent hardening (Kalidindi et al., 1992; Knezevic et al., 2016a, 2013b, 2013d; Peirce et al., 1982; Tabourot et al., 1997). Both self and latent hardening are included in the strength interaction matrix, which is also called the interaction matrix. The matrix describes the relative strength of various dislocation interactions. These interactions can be similar for a wide range of alloys with the same crystal structure. The latent hardening coefficients are most often calibrated to fit multiple stress-strain curves of a studied material. The values in the matrix can also be measured experimentally (Franciosi et al., 1980; Jackson and Basinski, 1967; Kocks and Brown, 1966; Wu et al., 1991b) or calculated using dislocation dynamics (Devincre et al., 2008; Kubin et al., 2008b; Madec et al., 2003).

Numerical issues with the incorporation of latent hardening in crystal plasticity models have been observed in literature (Ortiz and Repetto, 1999; Peirce et al., 1982). Specifically, the incorporation of the theory 1 of latent hardening in the elasto-plastic self-consistent (EPSC) formulation (Turner and Tomé, 1994) of interest in the present work requires the development of a new approach due to the singularities arising from the SC Eshelby solution procedure. Moreover, the solution procedure for single crystal stress increment needs to be advanced. The objectives of the present paper are to: (1) enable a crystallographic hardening law within EPSC homogenization (Zecevic and Knezevic, 2015; Zecevic et al., 2016a) to consider the physics of latent hardening, (2) reveal the origin of plastic anisotropy in AA6022-T4 by modeling the effects of latent hardening, and (3) predict the characteristics of large strain cyclic deformation for the material.

2. Material

This study is carried out on AA6022-T4 alloy, which is an important age-hardenable aluminum alloy exhibiting an excellent combination of strength and ductility (Alcoa). The typical chemical composition of the alloy in wt. % is 1.21 Si, 0.56 Mg, 0.12 Fe, 0.08 Mn, and 0.05 Cu, balanced with Al. The AA6022 alloy can have a certain amount of precipitates, depending on the aging treatment (Anjabin et al., 2014; Gupta et al., 2001; Miao and Laughlin, 1999). The precipitates, together with solutes, impede dislocation motion (Rauch et al., 2002). Since AA6022-T4 does not undergo artificial aging, the content of precipitates is small. The response is measured in simple tension along the rolling direction (RD), at 45° with respect to RD, and the transverse direction (TD) (Tian et al., 2016; Zecevic et al., 2016b). Several tests were carried out per test direction and the recorded curves were within a spread of 2%. The alloy exhibits a classic decreasing hardening rate, which is similar to many materials deforming by crystallographic slip. Evidently, the plastic anisotropy evolves with plastic strain. The r-ratio, defined as the ratio between the in-plane plastic strain in the direction perpendicular to the loading direction and the plastic strain in the through-thickness normal direction (ND), is plotted as a function of plastic strain in the loading direction in Fig. 2b.

The initial crystallographic texture of the alloy was measured using electron backscattered diffraction (EBSD) over a large area and is shown in Fig. 2c using the pole figures visualization. It predominantly contains a cube texture component spread of moderate intensity. The average grain size in the material is estimated from EBSD scans to be approximately 44 μm.

The alloy was also tested under the cycle tension-compression along the RD to four levels of true strain: 0.01, 0.05, 0.1 and 0.15 (Fig. 2d), as reported in (Barrett et al., 2017). The testing setup for acquiring such data was explained in our earlier work (Zecevic et al., 2016a). The macroscopic characteristic of the alloy behavior upon unloading is the existence of a very short initial linear portion followed by a larger non-linear unloading portion, which is further followed by a drop in yield stress relative to that reached at the end of forward straining. The phenomenon is known as the Bauschinger effect (BE) (Bauschinger, 1886). Subsequently, the hardening rate in compression is different from the hardening rate during forward tension. As a result, the alloy exhibits what is known as the permanent softening behavior (Hasegawa et al., 1975), which is governed by the annihilation of dislocations during compression in the reverse direction.

3. Elasto-plastic self-consistent formulation

The modeling framework presented in this work is intended for understanding material behavior and simulations of metal

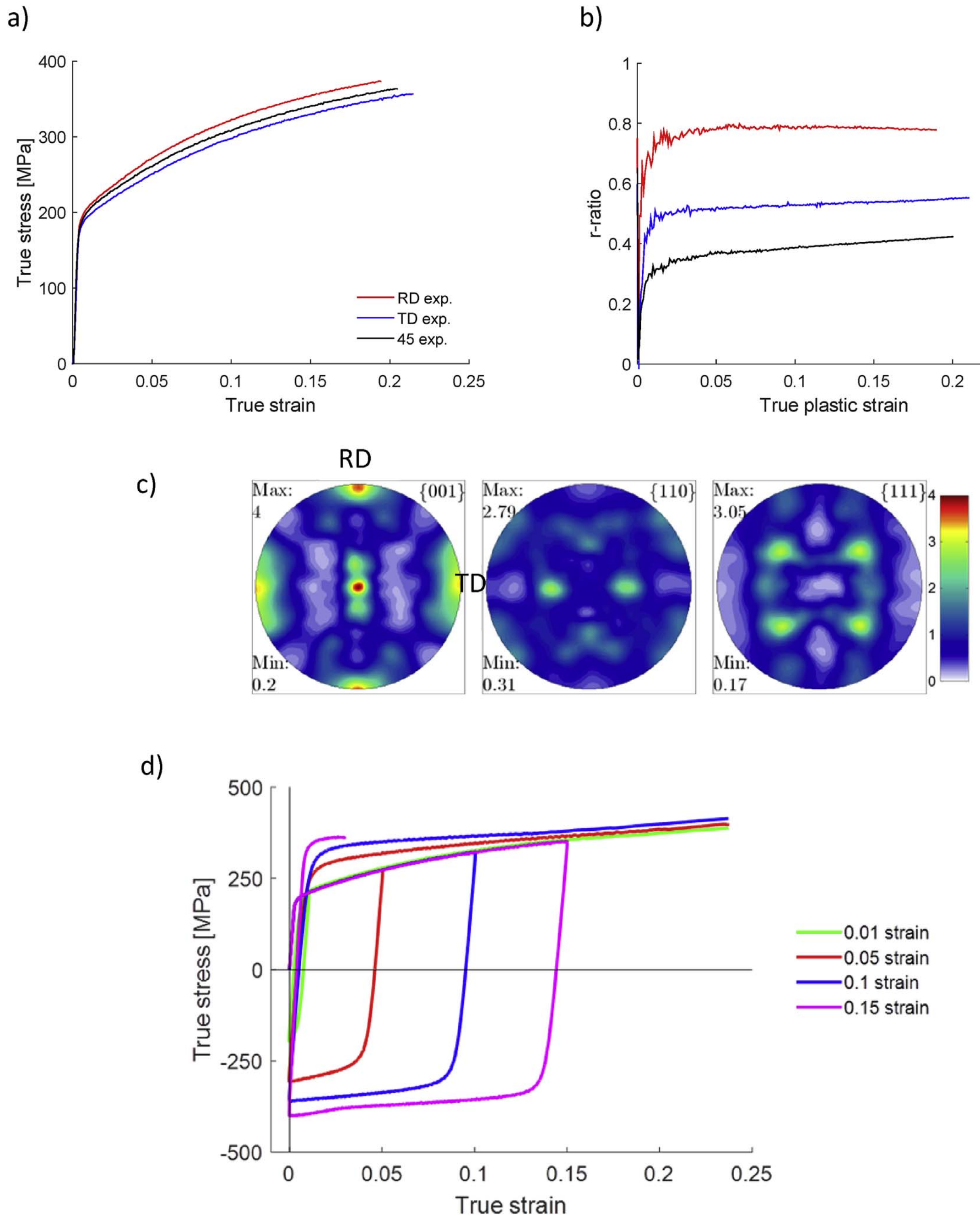

Fig. 2. Mechanical response and initial texture of AA6022-T4 alloy: (a) true stress-true strain response in simple tension along RD, TD, and at 45° with respect to RD, (b) evolution of r-ratio with plastic strain during simple tension along RD, TD, and at 45° with respect to RD, (c) pole figures showing the initial texture, and (d) large strain cyclic tension-compression response measured along the RD.

forming, which subject metals to large plastic strains developing highly non-uniform stress-strain fields (Al-Harbi et al., 2010; Hosford and Caddell, 2011; Jahedi et al., 2014, 2015b; Wagoner et al., 2013; Zecevic et al., 2015b, c; Zecevic et al., 2016b). These fields are intra- and inter-granular heterogeneities and play a significant role during strain-path changes and unloading (Bauschinger, 1886; Knezevic et al., 2013a; Pavlina et al., 2015). The EPSC model was originally developed in (Neil et al., 2010; Turner and Tomé, 1994; Wollmershauser et al., 2012). Below, we provide a summary of the EPSC model.

In the description that follows, "·" will represent a dot product, "⊗" will represent a tensor product, and α will be used to denote a family of slip systems while s will denote individual slip systems belonging to the family. The self-consistent scheme is based on an equivalent inclusion method where each grain is treated as an ellipsoidal inclusion inside the homogeneous equivalent medium (HEM) i.e. the polycrystalline matrix. The mechanics of the inclusion is solved using a Green's function approach. Since individual grains interact only with HEM, the overall model is referred to as a one-site model. Each grain comprising a polycrystal has a crystal lattice orientation, an ellipsoidal shape, and a volume fraction. The former two evolve with plastic strain. The matrix has unknown tangent stiffness which is to be determined by enforcing the macroscopic stress and strain rate to be volume averages of the corresponding single crystal quantities:

$$\hat{\boldsymbol{\sigma}} = <\hat{\boldsymbol{\sigma}}^c>; \quad \dot{\boldsymbol{\varepsilon}} = <\dot{\boldsymbol{\varepsilon}}^c>. \tag{3}$$

In Eq. (3), the polycrystal Jaumann stress rate and strain rate are expressed as the volume average of the corresponding grain, c, quantities. These macroscopic quantities are linked using:

$$\hat{\boldsymbol{\sigma}} = \mathbf{L}\dot{\boldsymbol{\varepsilon}}, \tag{4}$$

where $\mathbf{L}$ is the unknown instantaneous elasto-plastic stiffness four-rank tensor calculated iteratively using the SC procedure (Eshelby, 1957; Turner and Tomé, 1994). The Cauchy stress rate is related to the Jaumann stress rate using (Zecevic et al., 2017a):

$$\dot{\boldsymbol{\sigma}} = \hat{\boldsymbol{\sigma}} + <\mathbf{W}^c\boldsymbol{\sigma}^c> - <\boldsymbol{\sigma}^c\mathbf{W}^c> = \mathbf{L}\dot{\boldsymbol{\varepsilon}} + <\mathbf{W}^c\boldsymbol{\sigma}^c> - <\boldsymbol{\sigma}^c\mathbf{W}^c>, \tag{5}$$

where $\mathbf{W}^c$ is an elastic spin per grain, c, which will be defined shortly. Equation (5) is integrated over straining time explicitly for obtaining the macroscopic Cauchy stress. The local strain rate per crystal, c, and the overall strain rate are related using a localization tensor:

$$\dot{\boldsymbol{\varepsilon}}^c = \mathbf{A}^c\dot{\boldsymbol{\varepsilon}}. \tag{6}$$

The localization tensor for a given instantaneous local elasto-plastic stiffness $\mathbf{L}^c$ is

$$\mathbf{A}^c = \left(\mathbf{L}^c + \mathbf{L}^{c^*}\right)^{-1}\left(\mathbf{L}^{c^*} + \mathbf{L}\right), \tag{7}$$

where, $\mathbf{L}^{c^*} = \mathbf{L}((\mathbf{S}^c)^{-1} - \mathbf{I})$ is the effective stiffness from the interaction equation: $(\hat{\boldsymbol{\sigma}}^c - \hat{\boldsymbol{\sigma}}) = -\mathbf{L}^{c^*}(\dot{\boldsymbol{\varepsilon}}^c - \dot{\boldsymbol{\varepsilon}})$. $\mathbf{S}^c$ is the symmetric portion of the Eshelby tensor while $\mathbf{I}$ is a fourth rank identity. Finally, the above relations result in an implicit equation for macroscopic (matrix) tangent stiffness:

$$\mathbf{L} = <\mathbf{L}^c\mathbf{A}^c><\mathbf{A}^c>^{-1}. \tag{8}$$

At the grain/local level, the constitutive relation is:

$$\hat{\boldsymbol{\sigma}}^c = \mathbf{C}^c\left(\dot{\boldsymbol{\varepsilon}}^c - \sum_s \mathbf{m}^{c,s}\dot{\gamma}^{c,s}\right) - \boldsymbol{\sigma}^c tr(\dot{\boldsymbol{\varepsilon}}^c), \tag{9}$$

where $\mathbf{C}^c$ is the fourth rank elastic stiffness tensor, $\sum_s \mathbf{m}^{c,s}\dot{\gamma}^{c,s}$ is the plastic strain rate made up of slip system shearing rates, $\dot{\gamma}^{c,s}$, and $\mathbf{m}^{c,s} = 0.5(\mathbf{b}^{c,s} \otimes \mathbf{n}^{c,s} + \mathbf{n}^{c,s} \otimes \mathbf{b}^{c,s})$, where $\mathbf{b}^{c,s}$ and $\mathbf{n}^{c,s}$ are the slip system direction and plane normal, respectively.

To activate a slip system s, a resolved shear stress on it lowered by backstress, $\tau_{bs}^{c,s}$, must reach its slip resistance, $\tau_c^{c,s}$, i.e. $\mathbf{m}^{c,s}\cdot\boldsymbol{\sigma}^c - \tau_{bs}^{c,s} = \tau_c^{c,s}$ and the stress has to remain on the evolving crystal yield surface i.e., $\mathbf{m}^{c,s}\cdot\hat{\boldsymbol{\sigma}}^c - \dot{\tau}_{bs}^{c,s} = \dot{\tau}_c^{c,s}$. The slip resistance defines single crystal yield surface. The addition of the backstress term introduces kinematic hardening effects at a slip system level. Therefore, single crystal yield surface expands with deformation as defined with the slip resistance term, $\tau_c^{c,s}$, and moves as defined with the backstress term, $\tau_{bs}^{c,s}$. Note that slip systems are doubled because the two opposite shearing senses are counted separately.

The slip resistance and backstress evolve with the shearing rates using:

$$\dot{\tau}_c^{c,s} = \sum_{s'} h^{ss'}\dot{\gamma}^{c,s'}, \tag{10}$$

$$\dot{\tau}_{bs}^{c,s} = \sum_{s'} h_{bs}^{ss'}\dot{\gamma}^{c,s'}, \tag{11}$$

where $h^{ss'}$ and $h_{bs}^{ss'}$ are the hardening matrix and the backstress matrix, respectively, whose expressions depend on the adopted hardening and backstress evolution laws. The $h^{ss'}$ and $h_{bs}^{ss'}$ need to be pre-determined in order to solve the elasto-plastic self-consistent problem. They can either be constant or defined as a function of state variables. For our purpose, we consider $h^{ss'}$ and $h_{bs}^{ss'}$ to be functions of accumulated shear strain on slip systems, γ^s. The expressions for $h^{ss'}$ and $h_{bs}^{ss'}$ are defined in the following sections. Finally, the crystal constitutive law is:

$$\hat{\boldsymbol{\sigma}}^c = \mathbf{L}^c\dot{\boldsymbol{\varepsilon}}^c, \tag{12}$$

where $\mathbf{L}^c$ is:

$$\mathbf{L}^c = \mathbf{C}^c - \mathbf{C}^c\sum_s \mathbf{m}^{c,s} \otimes \left(\sum_{s'} (X^{ss'})^{-1}\mathbf{m}^{c,s'}(\mathbf{C}^c - \boldsymbol{\sigma}^c \otimes \mathbf{i})\right) - \boldsymbol{\sigma}^c \otimes \mathbf{i}, \tag{13}$$

with:

$$X^{ss'} = h^{ss'} + h_{bs}^{ss'} + \mathbf{C}^c\cdot\mathbf{m}^{c,s} \otimes \mathbf{m}^{c,s'}. \tag{14}$$

Note that indices s and s’ in Eqs. (13) and (14) go only over active slip systems. Therefore, while full hardening and backstress matrices are used for updating slip resistance and backstress, only a portion of them is used for the calculation of tangent stiffness.

The grain spin tensor necessary for texture evolution, $\mathbf{W}^c$, is:

$$\mathbf{W}^c = \mathbf{W}^{app} + \mathbf{\Pi}^c - \mathbf{W}^{p,c}, \tag{15}$$

where $\mathbf{W}^{app}$ is the applied spin, $\mathbf{\Pi}^c$ is the spin calculated from an applied macroscopic strain rate to the polycrystal and the anti-symmetric part of the Eshelby tensor for grain c (Lebensohn and Tomé, 1993), and $\mathbf{W}^{p,c}$ is the plastic spin. The plastic spin is:

$$\mathbf{W}^{p,c} = \sum_s \mathbf{q}^{c,s}\dot{\gamma}^{c,s}, \tag{16}$$

where $\mathbf{q}^{c,s} = 0.5(\mathbf{b}^{c,s} \otimes \mathbf{n}^{c,s} - \mathbf{n}^{c,s} \otimes \mathbf{b}^{c,s})$.

3.1. Dislocation-based hardening law incorporating latent hardening

We use the notation which distinguishes between arbitrarily chosen positive $s+$ and negative s-directions of slip systems, while the index s refers to both directions. Dislocation-based strain rate and temperature sensitive hardening law is used to evolve slip resistance (Beyerlein and Tomé, 2008; Jahedi et al., 2015a; Knezevic et al., 2012, 2014a, 2014b, 2015). The dislocation-based hardening law was implemented within EPSC first in (Zecevic et al., 2015a) and used in several other studies (Lentz et al., 2015; Nugmanov et al., 2018; Risse et al., 2017). The slip resistance is defined as:

$$\tau_c^s = \tau_0^\alpha + \tau_{forest}^s + \tau_{debris}^\alpha, \tag{17}$$

where:

$$\tau_{forest}^s = b^\alpha \chi \mu^\alpha \sqrt{\sum_{s'} L^{ss'} \rho_{tot}^{s'}} \tag{18}$$

$$\tau_{debris}^\alpha = k_{deb} \mu^\alpha b^\alpha \sqrt{\rho_{deb}}\, log\left(\frac{1}{b^\alpha \sqrt{\rho_{deb}}}\right) \tag{19}$$

where τ_0^α is an initial slip resistance including: the Peierls stress, solid solution contribution, precipitation contribution, and the Hall-Petch-like effect, τ_{forest}^s is a forest term arising from statistically stored dislocations, τ_{debris}^α is a debris term coming from dislocations stored as debris. $b^\alpha = 2.86\ 10^{-10}$ m is the Burgers vector, $\chi = 0.9$ is an interaction constant, ρ_{tot}^s is the total forest dislocation density for *sth* slip system ($s \in \alpha$) and $L^{ss'}$ is a latent hardening matrix aka a strength interaction matrix (Franciosi and Zaoui, 1982; Khadyko et al., 2016). Magnitude of off-diagonal entries in the strength interaction matrix, $L^{ss'}$, controls the magnitude of the off-diagonal entries in the hardening matrix, $h^{ss'}$. In Eq. (19), $k_{deb} = 0.086$ is a material independent constant and ρ_{deb} is the debris dislocation density (Madec et al., 2003).

Equation (18) is a modified Taylor relationship for the evolution of slip resistance accounting for dislocation densities on different slip systems and their interactions through the strength interaction matrix. Thus, the evolution of slip resistance depends on the accumulation of immobile dislocations and dislocation interactions. Both increase in dislocation density and dislocation interactions between some slip systems lead to a decrease of the mean free path. Previous study on anisotropy in AA6060 showed that the general trends of anisotropy in flow stress can be captured using latent hardening (Khadyko et al., 2016), where several different interaction matrices from the literature have been tested. A stronger latent hardening than the self-hardening is what all these interaction matrices have in common. However, the current EPSC formulation (for convenience, we will refer to this formulation as the standard EPSC) is unable to converge for such strength interaction matrices, due to the loss of ellipticity of the macroscopic tangent modulus. The issue is resolved in the present paper by proposing diagonalization of the hardening matrix, which will be described shortly.

The strength interaction matrix, $L^{ss'}$, has in general 24 x 24 elements, since each slip system within {111}<1$\bar{1}$0> family of 12 slip systems has positive, s^+, and negative, s^-, direction, which are treated independently. Components of the strength interaction matrix describe different dislocation interactions, which will be described later. The coefficients of the strength interaction matrix can be evaluated experimentally or by use of dislocation dynamics and atomistic simulations (Franciosi et al., 1980; Madec et al., 2003). The strength interaction matrix is constant and does not evolve with deformation.

Thus far, slip resistance has been defined in terms of the total forest and debris dislocation densities. Next, an evolution law for dislocation densities in terms of shear strain on slip systems is defined. The evolution of total forest dislocation density during reversed loading takes a different form than the one during forward loading. The origin of altered evolution law during reversal is the annihilation of portion of stored dislocations. The evolution laws for dislocation densities, which take into account annihilation of stored dislocations during load reversal, have been developed in (Kitayama et al., 2013; Rauch et al., 2007). The dislocation evolution laws from (Kitayama et al., 2013) have been implemented into EPSC hardening law in our previous works (Zecevic and Knezevic, 2015). The total dislocation density is written as:

$$\rho_{tot}^s = \rho_{for}^s + \rho_{rev}^{s^+} + \rho_{rev}^{s^-}, \tag{20}$$

where ρ_{for}^s is the forward dislocation density and $\rho_{rev}^{s^+}$ and $\rho_{rev}^{s^-}$ are the reversible dislocation densities associated with the s^+ and s^- directions, respectively. The three dislocation densities are evolved as functions of shear strain and shearing direction (Khadyko et al., 2016; Kitayama et al., 2013; Kocks and Mecking, 1981):

$$\left(\text{if } d\gamma^{s^+} > 0\right)$$

$$\frac{\partial \rho^s_{for}}{\partial \gamma^s} = (1-p)k_1^\alpha \sqrt{\sum_{s'} g^{ss'}\rho^{s'}_{tot}} - k_2^\alpha(\dot{\varepsilon}, T)\rho^s_{for}, \tag{21a}$$

$$\frac{\partial \rho^{s^+}_{rev}}{\partial \gamma^s} = pk_1^\alpha \sqrt{\sum_{s'} g^{ss'}\rho^{s'}_{tot}} - k_2^\alpha(\dot{\varepsilon}, T)\rho^{s^+}_{rev}, \tag{22a}$$

$$\frac{\partial \rho^{s^-}_{rev}}{\partial \gamma^s} = -k_1^\alpha \sqrt{\sum_{s'} g^{ss'}\rho^{s'}_{tot}}\left(\frac{\rho^{s^-}_{rev}}{\rho^s_0}\right)^m, \tag{23a}$$

$$\left(\text{if } d\gamma^{s^-} > 0\right)$$

$$\frac{\partial \rho^s_{for}}{\partial \gamma^s} = (1-p)k_1^\alpha \sqrt{\sum_{s'} g^{ss'}\rho^{s'}_{tot}} - k_2^\alpha(\dot{\varepsilon}, T)\rho^s_{for}, \tag{21b}$$

$$\frac{\partial \rho^{s^+}_{rev}}{\partial \gamma^s} = -k_1^\alpha \sqrt{\sum_{s'} g^{ss'}\rho^{s'}_{tot}}\left(\frac{\rho^{s^+}_{rev}}{\rho^s_0}\right)^m, \tag{22b}$$

$$\frac{\partial \rho^{s^-}_{rev}}{\partial \gamma^s} = pk_1^\alpha \sqrt{\sum_{s'} g^{ss'}\rho^{s'}_{tot}} - k_2^\alpha(\dot{\varepsilon}, T)\rho^{s^-}_{rev}, \tag{23b}$$

with the following initial conditions:

$$\rho^s_{for}(\gamma^s = 0) = 10^{11}\, m^{-2}, \quad \rho^{s^+}_{rev}(\gamma^s = 0) = 0 \quad \text{and } \rho^{s^-}_{rev}(\gamma^s = 0) = 0, \tag{24}$$

where k_1^α is a coefficient controlling the rate of generation of statistically stored dislocations, k_2^α is a rate-sensitive coefficient for dynamic recovery (Beyerlein and Tomé, 2008), p is a reversibility parameter having a value between 0 and 1, and $g^{ss'}$ is another interaction matrix, which defines the strength of dislocation interaction governing solely the accumulation of forest dislocations on slip system s depending on the dislocation density on system s'. Analogy between $L^{ss'}$ for slip resistance to $g^{ss'}$ for the rate of dislocation evolution is evident. The interaction matrix for dislocation storage is a constant matrix and is inspired by the previous works (Khadyko et al., 2016; Kocks et al., 1991; Teodosiu and Raphanel, 1991). The $g^{ss'}$ is a constant matrix not expected to evolve with deformation. The effect of entries of $g^{ss'}$ matrix on mechanical response is discussed in results section. Note that $g^{ss'}$ does not create off-diagonal terms in hardening matrix, $h^{ss'}$. The reversibility parameter controls the fraction of total dislocation density that evolves as reversible dislocation density. In Eqs. (22b) and (23a), m is a parameter accounting for the rate of dislocation recombination having value of 0.5 (Wen et al., 2015) and ρ^s_0 is the total dislocation density at the moment of shear reversal on the *sth* slip system (Kitayama et al., 2013).

The rate-sensitive coefficient for dynamic recovery, k_2^α, is:

$$\frac{k_2^\alpha}{k_1^\alpha} = \frac{\chi b^\alpha}{g^\alpha}\left(1 - \frac{k_B T}{D^\alpha (b^\alpha)^3} ln\left(\frac{\dot{\varepsilon}}{\dot{\varepsilon}_0}\right)\right), \tag{25}$$

where, k_B, $\dot{\varepsilon}_0$, g^α and D^α are the Boltzmann constant, a reference strain rate taken to be $10^7\ s^{-1}$, an effective activation enthalpy and a drag stress, respectively. The evolution law for debris dislocation density is:

$$\frac{\partial \rho_{deb}}{\partial \gamma^s} = q^\alpha b^\alpha \sqrt{\rho_{deb}}\, k_2^\alpha(\dot{\varepsilon}, T)\rho^s_{tot}, \tag{26}$$

where q^α is a dislocation recovery rate constant that extracts a fraction of α-type dislocations that do not annihilate but become debris from those that do annihilate. Initial content of debris dislocation density is taken to be 0.1 m^{-2}.

3.2. Backstress evolution law

To also aid in capturing the effect of strain path reversal, the slip system backstress evolution is considered, using an empirical law. The implementation of a backstress law in EPSC was first presented in (Wollmershauser et al., 2012). Here we consider an evolution law for backstress per slip system based on the work presented in (Beyerlein and Tomé, 2007; Zecevic et al., 2016a). In the empirical formulation employed here, we first define slip system sources of backstress which evolve with shear strain. All sources of backstresses on individual slip systems are superimposed to form the backstress tensor as proposed in (Harder, 1999). The backstress tensor is then projected on individual slip systems to arrive to the final expression of backstress. The final expression for backstress on a slip system τ^s_{bs}, is:

$$\tau_{bs}^{s} = \mathbf{m}^{s}\cdot\boldsymbol{\sigma}_{bs}^{c} = \tau_{bs,sys}^{s} + 2\sum_{s'} \mathbf{m}^{s}\cdot\mathbf{m}^{s'}\tau_{bs,sys*}^{s'}, \tag{27}$$

with

$$\tau_{bs,sys*}^{s'} = \begin{cases} \tau_{bs,sys}^{s'} & if\ \tau_{bs,sys}^{s'} > 0 \\ 0 & if\ \tau_{bs,sys}^{s'} < 0 \end{cases} \tag{28}$$

where $\boldsymbol{\sigma}_{bs}^{c}$ is backstress tensor formed by superimposing slip system sources of backstress, $\tau_{bs,sys}^{s'}$, and the sum over s' spans over all slip systems and $s' \neq s$. We adopt following functions for the evolution of $\tau_{bs,sys}^{s}$ with shear strain:

(if $d\gamma^{s^+} > 0$ and $\tau_{bs,sys}^{s^+} > 0$)

$$\tau_{bs,sys}^{s^+} = \tau_{bs}^{sat}\left(1 - \exp\left(-\nu\gamma^{s^+}\right)\right), \tag{29}$$

$$\tau_{bs,sys}^{s^-} = -A\tau_{bs,sys}^{s^+}, \tag{30}$$

(if $d\gamma^{s^+} > 0$ and $\tau_{bs,sys}^{s^+} < 0$)

$$\tau_{bs,sys}^{s^+} = -(A+1)\tau_{bs}^{sat}\exp\left(-\frac{\gamma^{s^-}}{\gamma_b}\right) + \tau_{bs}^{sat} \tag{31}$$

$$\tau_{bs,sys}^{s^-} = -\frac{1}{A}\tau_{bs,sys}^{s^+} \tag{32}$$

where τ_{bs}^{sat} is a saturation value for backstresses, A is a parameter for asymmetric evolution of backstress on a slip system in two different directions s+ and s-, γ_b and ν are material parameters. The shear strain γ^{s} is recorded from the point of local load reversal.

3.3. *Analytical description of the hardening matrix, $h^{ss'}$, and the backstress matrix $h_{bs}^{ss'}$*

To complete the set of relations pertaining to the EPSC formulation, the hardening matrix $h^{ss'}$, and the backstress matrix, $h_{bs}^{ss'}$, remain to be defined. Assuming that the functions defining the evolution of slip resistance and backstress with shear strain exist, from Eqs. (10) and (11) it follows that entries of the hardening and backstress matrices are the following partial derivatives:

$$h^{ss'} = \frac{\partial\tau_{c}^{s}}{\partial\gamma^{s'}};\ h_{bs}^{ss'} = \frac{\partial\tau_{bs}^{s}}{\partial\gamma^{s'}}. \tag{33}$$

The expressions for and $h_{bs}^{ss'}$ are provided in appendix A for the evolution laws used in the present study.

3.4. *Solution procedure for single crystal stress increment after introducing effects of latent hardening*

The latent hardening is introduced in the model through the use of the strength interaction matrix, $L^{ss'}$, in Eq (18). The strength interaction matrix affects the hardening matrix, $h^{ss'}$ (appendix A). More specifically, it affects the ratio between elements on the diagonal to the off-diagonal elements in $h^{ss'}$ for active slip systems. The positive definiteness of the hardening matrix is a necessary condition for the determination of shear rates on active slip system in rate independent formulation (Hill, 1966). However, the positive definiteness of $h^{ss'}$ is not expected when latent hardening is stronger than self-hardening, since the largest elements of the matrix are not on the diagonal (Golub and Loan, 1996).

The realistic (experimentally measured) latent hardening constants as presented in the literature for Al and Al alloys (Franciosi et al., 1980; Khadyko et al., 2016; Kocks and Brown, 1966) result in larger latent hardening than self-hardening. As a result, computational issues arise both at single crystal and polycrystalline levels. In this section, the single crystal issues are treated, while in the next section we treat issues at polycrystal level.

The single crystal solution procedure involves the determination of a set of active slip systems and shear increments on active slip systems given an imposed single crystal increment in strain. The procedure begins by determining a set of potentially active slip systems fulfilling the loading condition $\mathbf{m}^{s}\cdot\boldsymbol{\sigma}^{c} - \tau_{bs}^{s} = \tau_{c}^{s}$. Next, shear increments are determined for all potentially active slip systems by enforcing the consistency condition, $\mathbf{m}^{s}\cdot\hat{\boldsymbol{\sigma}}^{c} - \dot{\tau}_{bs}^{s} = \dot{\tau}_{c}^{s}$, producing the system of linear equations:

$$\sum_{s'}\left(h^{ss'} + h_{bs}^{ss'} + \mathbf{C}^{c}\cdot\mathbf{m}^{s}\otimes\mathbf{m}^{s'}\right)\Delta\gamma^{s'} = \mathbf{m}^{s}(\mathbf{C}^{c} - \boldsymbol{\sigma}^{c}\otimes\mathbf{i})\Delta\boldsymbol{\varepsilon}^{c}. \tag{34}$$

Evidently, the matrix, $X^{ss'}$, defined in Eq. (14) needs to be inverted in order to solve for shear increments, $\Delta\gamma^{s'}$, on potentially active slip systems. If any of the resulting shear increments is negative, then that slip system is removed from the set of potentially active slip systems and shear increments are recalculated. Slip systems are eliminated from the initial set of potentially active slip systems until all active slip systems have positive shear increments. In addition, inactive slip systems must satisfy $\mathbf{m}^{s}\cdot\boldsymbol{\sigma}^{c} - \tau_{bs}^{s} \leq \tau_{c}^{s}$, i.e. stress cannot get out of the single crystal yield surface. The final set of active slip systems is used in calculating the tangent stiffness of single crystals (Eq. (13)).

Two possible issues can arise in the above presented procedure. The first issue is singularity of the matrix $X^{ss'}$. The problem has been treated in literature (Anand and Kothari, 1996; Ben Bettaieb et al., 2012; Knockaert et al., 2000; Mánik and Holmedal, 2014; Schröder and Miehe, 1997). We adopt the approach of (Anand and Kothari, 1996), where a singular value decomposition procedure of $X^{ss'}$ is proposed:

$$\mathbf{X} = \mathbf{U}\mathbf{W}\mathbf{V}^T \tag{35}$$

where $\mathbf{U}$ and $\mathbf{V}$ are orthogonal matrices, while $\mathbf{W}$ is a diagonal matrix with singular values of $\mathbf{X}$ positioned along the diagonal. The pseudo inverse of matrix $\mathbf{X}^{+}$ is then:

$$\mathbf{X}^{+} = \mathbf{V}\mathbf{W}^{+}\mathbf{U}^T \tag{36}$$

where $\mathbf{W}^{+}$ is diagonal matrix given with:

$$(W^{+})^{ss} = \begin{cases} 1/W^{ss} & if \quad W^{ss}/\max W^{ss} > 1e-12 \\ 0 & if \quad W^{ss}/\max W^{ss} < 1e-12 \end{cases}. \tag{37}$$

The second issue that rarely occurs is inability to find a set of active slip systems satisfying all constraints for an arbitrary hardening law. We observe that in some cases the elimination of slip systems with negative shear increments violates the condition $\mathbf{m}^s \cdot \boldsymbol{\sigma}^c - \tau^s_{bs} \le \tau^s_c$ for some of the eliminated slip systems at the end of the applied increment. A couple of percent of all active slip systems can exhibit this problem with introduction of latent hardening more pronounced than self-hardening. The percent of slip systems where stress exits the single crystal yield surface is dependent on adopted interaction matrix for dislocation density evolution, $g^{ss'}$, and strength interaction matrix, $L^{ss'}$. If stress exits the yield surface on some slip systems, the slip resistance is corrected so that stress remains on the single crystal yield surface i.e. slip resistance is enforced to be $\tau^s_c = \mathbf{m}^s \cdot \boldsymbol{\sigma}^c - \tau^s_{bs}$.

3.5. Singularity in the Eshelby tensor calculation upon introducing effects of latent hardening

Using the methods presented in the previous section, solution to single crystals can be found for a given hardening law. However, issues are also encountered within the homogenization procedure, i.e. in the Eshelby tensor calculation.

The general symmetric Eshelby tensor, defining the strain rate inside the inclusion, can be calculated in terms of the Green's function (Lebensohn et al., 1998). The Green's function in Fourier space is calculated using:

$$k^2 \hat{G}_{in} = (\alpha_l \alpha_j L_{ijnl})^{-1}, \tag{38}$$

where $\hat{G}_{in}$ is the Green's function in Fourier space and $\mathbf{k}$ is a point vector of the Fourier space with magnitude k and in direction of a unit vector $\boldsymbol{\alpha} = (\sin\theta\cos\varphi, \sin\theta\sin\varphi, \cos\theta)$ (i.e. $\mathbf{k} = k\boldsymbol{\alpha}$).

The possible issue in the Eshelby tensor calculation is singularity of the 2nd rank tensor $\alpha_l \alpha_j L_{ijnl}$ for certain values of the angles θ and φ, over which integration is performed to define the Eshelby tensor in real space. This condition can be expressed as:

$$\det(\alpha_l \alpha_j L_{ijnl}) = 0, \tag{39}$$

which is referred to as the loss of elipticity of the tangent stiffness and can be related to bifurcation and/or shear band formation (Franz et al., 2009). In contrast, the strong elipticity of tangent stiffness is desirable and defined as:

$$L_{ijnl} x_i y_j x_n y_l = (L_{ijnl} y_j y_l) x_i x_n = Q_{in} x_i x_n > 0, \tag{40}$$

where Q_{in} is the acoustic tensor (Merodio and Ogden, 2003) and x_i and y_j are arbitrary unit vectors. For L_{ijnl} to be strongly elliptical, the acoustic tensor needs to be positive definite, which implies that $\det Q_{in} \ne 0$ (Merodio and Ogden, 2003). The strong ellipticity of the tangent stiffness is a necessary condition for solvability of the equivalent inclusion problem for an ellipsoidal inhomogeneity (Freidin and Kucher, 2015). If the differential equations of equilibrium are elliptic, the condition of strong ellipticity is satisfied.

We notice that tangent stiffness loses ellipticity when the latent hardening is more pronounced than the self-hardening. This implies that the use of the theory 1 of latent hardening leads to loss of ellipticity, while the use of the theory 2 of latent hardening does not cause the loss of elipticity because the matrix is diagonal. The same effect of the theory 1 latent hardening on the loss of ellipticity of governing equations for single crystals was noted in (Peirce et al., 1982). Similar issues are encountered in the case of simulating softening in materials (Nguyen, 2005). Problems with the loss of ellipticity can be avoided by introducing the rate-dependence i.e. visco-plasticity (Needleman, 1988; Peirce et al., 1983). Introducing strain rate sensitivity in the rate-independent framework of EPSC is left for future developments.

The loss of strong ellipticity condition for overall tangent stiffness of a polycrystal appears to be related to the loss of ellipticity of single crystals tangent stiffness tensors constituting the polycrystal. Therefore, before investigating the overall tangent stiffness tensor, we investigate the behavior of tangent stiffness tensors of single crystals in function of the ratio between diagonal and off-diagonal terms in their respective hardening matrices.

A crystal with Bunge-Euler angles (23, 12, 308) is arbitrarily chosen for the analysis. Four slip systems with the highest Schmid factor under tension along the direction 1 are assumed to be active in constructing the tangent stiffness, $\mathbf{L}^c$, according to Eqs. (13) and (14). The hardening matrix to facilitate the analysis is arbitrarily set to give a reasonable hardening rate as follows:

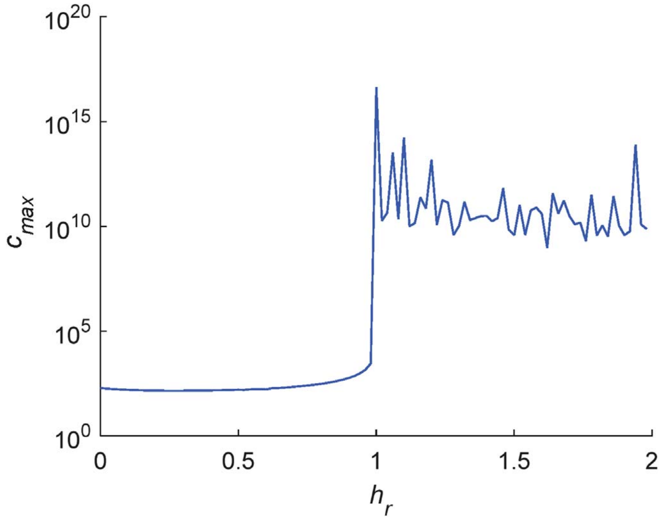

Fig. 3. Maximum condition number of acoustic tensor as a function of the ratio between diagonal and off-diagonal terms in the hardening matrix.

$$h^{ss'} = \begin{cases} 1000 & if\ s = s' \\ h_r 1000 & if\ s \neq s' \end{cases}, \tag{41}$$

where h_r defines the off-diagonal entries and s and s' go over active slip systems. The single crystal stress in Eq. (13) is assumed to be zero, while the single crystal elastic stiffness, $\mathbf{C}^c$, is based on the single crystal elastic constants for Al (Meyers and Chawla, 2009). We calculate the acoustic tensor of the single crystal tangent stiffness and its maximum condition number ($c_{\max}$). By definition, the condition number is the ratio between the largest and the smallest singular value of a matrix (Press et al., 1992). To achieve the maximum of the ratio, the vectors y_j and y_l in Eq. (40) are varied using the function 'fminunc' in Matlab to perform unconstrained optimization. Fig. 3 shows a plot of the condition number vs. h_r. Evidently, the acoustic tensor becomes near singular for $h_r > 1$. A similar conclusion for the behavior of single crystals was presented in (Peirce et al., 1982).

Next, we sample 200 crystals from the ODF shown in Fig. 2c and apply the hardening law given by Eq. (41). We set h_r to 1.5, the initial value of slip resistance to 50 MPa, and simulate simple tension of the polycrystal using EPSC. Fig. 4 shows the simulation results. The true stress-true strain curve (Fig. 4a) is plotted up to the strain level at which the EPSC is no longer able to solve for homogenized tangent stiffness. The fraction of grains having the max condition number of acoustic tensor greater than 1e8 is shown in Fig. 4b indicating that the number of grains losing ellipticity is increasing with strain. Our analysis shows that the macroscopic tangent stiffness has nearly lost ellipticity and therefore, the solution procedure in EPSC is breaking down. With further straining more grains would lose ellipticity and the overall tangent stiffness would lose ellipticity when nearly all grains lose their ellipticity (Franz et al., 2009).

From the above presented analysis, we conclude that the theory 1 description of latent hardening with experimentally evaluated

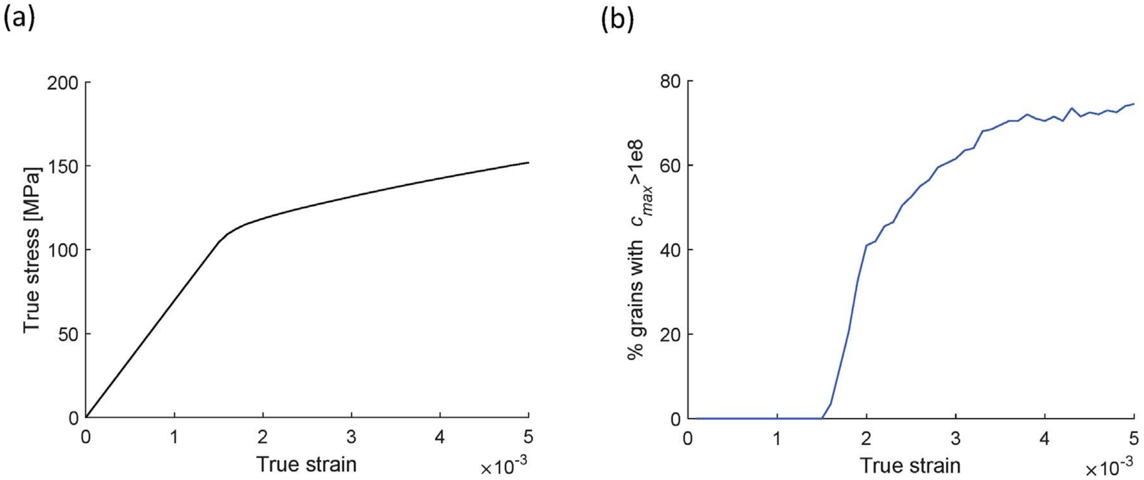

Fig. 4. (a) True stress-true strain curve calculated in simple tension for a polycrystal of 200 grains with a linear hardening law. (b) Evolution of % grains having the maximum condition number of acoustic tensor greater than 1e8 with strain.

latent hardening coefficients leads to the loss of ellipticity of the overall tangent stiffness.

3.6. Overcoming the loss of ellipticity

This section presents two methods used to suppress the loss of ellipticity, one proposed here and another available from the literature originally proposed to resolve the issue of non-uniqueness in the choice of active slip systems. The methods are based on opposing concepts in terms of the dependence of slip systems, as will become clear from the description below. Both methods have been compared against the latent hardening in the standard EPSC formulation for a case study in which the standard formulation converges. Results of the comparison suggest that the novel method proposed here is well suited for predicting the effect of latent hardening on plastic anisotropy of AA6022-T4.

3.6.1. Diagonalization of the hardening matrix procedure

In order to perform the homogenization procedure, the single crystal tangent stiffness needs to be elliptical. The ellipticity of tangent stiffness of single crystal is a function of relative size of diagonal and off-diagonal elements of the hardening matrix, as shown in Fig. 3. As stated earlier, the hardening matrix must be a positive definite. To resolve the problem we propose a replacement of the hardening matrix that enters the single crystal tangent stiffness calculation with a hardening matrix that is guaranteed to be positive definite. This matrix is referred to as the diagonalized hardening matrix.

Note that while the single crystal solution procedure involving a given hardening matrix remains as described in section 3.4, the diagonalized hardening matrix is inserted in Eqs. (14) and (13) for the calculation of single crystal tangent stiffness, $\mathbf{L}^c$.

The definition of new hardening matrix comes from assuming that both hardening matrices relate to the same hardening law, meaning that increments in slip resistance produced by both matrices should be the same:

$$\sum_{s'} h_r^{ss'} \Delta\gamma^{s'} = \sum_{s'} h^{ss'} \Delta\gamma^{s'} \tag{42}$$

where $h_r^{ss'}$ is the diagonalized hardening matrix. The indices s and s' in equation (42) go over active slip systems. The diagonalized matrix is written as:

$$h_r^{ss'} = h_d^{ss'} + r h_{off}^{ss'}, \tag{43}$$

where $h_d^{ss'}$ is the unknown matrix with off-diagonal elements equal to zero, $h_{off}^{ss'}$ is a matrix formed from $h^{ss'}$ by setting the matrix entries along the diagonal to zero and r is a diagonalization parameter set to a value between 0 and 1. The indices s and s' in equation (43) go over all slip systems. Replacing equation (43) in (42) allows determination of unknown elements along the diagonal of matrix $h_d^{ss'}$:

$$h_d^{ss} \Delta\gamma^s + \sum_{s'} r h_{off}^{ss'} \Delta\gamma^{s'} = \sum_{s'} h^{ss'} \Delta\gamma^{s'} \rightarrow h_d^{ss} = \frac{1}{\Delta\gamma^s}\left(\sum_{s'} h^{ss'} \Delta\gamma^{s'} - r \sum_{s'} h_{off}^{ss'} \Delta\gamma^{s'}\right). \tag{44}$$

where indices s and s' go over active slip systems. The diagonalization parameter, r, defines weight of the diagonal elements compared to off-diagonal elements. For instance, when $r = 1$ the matrix $h_r^{ss'}$ becomes $h^{ss'}$ i.e. off-diagonal elements are dominant, while when $r = 0$ the matrix $h_r^{ss'}$ becomes $h_d^{ss'}$ i.e. the matrix is diagonal.

Reducing hardening matrix to its diagonal form can be interpreted as "breaking the dependence" between slip systems in terms of slip resistance. The dependence of slip resistance is introduced by the concept of latent hardening theory 1, where slip resistance is dependent on shear on all slip systems and the hardening matrix is full.

While the proposed approach does not change the single crystal response, it affects the overall homogenized tangent stiffness. Therefore, the polycrystal response can be slightly altered. To evaluate the effect, we compare the results from this procedure with the results based on the regularized Schmid law (Gambin, 1992). The latter approach is summarized next.

3.6.2. Regularized Schmid law procedure

The regularized Schmid law for the rate-independent crystal plasticity was proposed in (Gambin, 1992). The formulation allows predictions of forming limit diagrams using the bifurcation analysis as presented in (Yoshida and Kuroda, 2012). Here we closely follow derivations from (Yoshida et al., 2009), while enforcing the normal to yield surface to have a norm of unity (Simo and Taylor, 1985). The rotation of single crystals is neglected for simplicity when deriving the equations and performing the integration. The single crystal yield function is:

$$f = \left(\sum_s \left(\frac{\boldsymbol{\sigma}^c \cdot \mathbf{m}^s}{\tau_c^s + \tau_{bs}^s}\right)^{2N}\right)^{\frac{1}{2N}} - 1 \le 0, \tag{45}$$

where N is an integer parameter controlling the radius of single crystal yield surface corners. With known yield function, the normal to yield surface is:

$$\hat{\mathbf{n}} = \left|\frac{\partial f(\boldsymbol{\sigma}^c)}{\partial \boldsymbol{\sigma}^c}\right|^{-1} \frac{\partial f(\boldsymbol{\sigma}^c)}{\partial \boldsymbol{\sigma}^c} = \frac{1}{\left|\sum_{\mathbf{s}}\left(\frac{\boldsymbol{\sigma}^{\mathbf{c}}\cdot\mathbf{m}^{\mathbf{s}}}{\tau_{\mathbf{c}}^{\mathbf{s}}+\tau_{\mathbf{bs}}^{\mathbf{s}}}\right)^{\mathbf{2N-1}}\frac{\mathbf{1}}{\tau_{\mathbf{c}}^{\mathbf{s}}+\tau_{\mathbf{bs}}^{\mathbf{s}}}\mathbf{m}^{\mathbf{s}}\right|}\sum_{s}\left(\frac{\boldsymbol{\sigma}^{c}\cdot\mathbf{m}^{s}}{\tau_c^s+\tau_{bs}^s}\right)^{2N-1}\frac{1}{\tau_c^s+\tau_{bs}^s}\mathbf{m}^s. \tag{46}$$

The plastic strain rate is:

$$\dot{\varepsilon}^{pl} = \dot{\Lambda}\hat{\mathbf{n}}, \tag{47}$$

where $\dot{\Lambda}$ is the plastic multiplier. Using the expression for plastic strain rate in terms of shear rates, $\dot{\varepsilon}^{pl} = \sum_s \dot{\gamma}^s\mathbf{m}^s$, together with Eqs. (46) and (47) we can express the shear rate as:

$$\dot{\gamma}^s = \dot{\Lambda}\hat{n}^s, \tag{48}$$

where:

$$\hat{n}^s = \frac{1}{\left|\sum_{\mathbf{s}}\left(\frac{\boldsymbol{\sigma}^{\mathbf{c}}\cdot\mathbf{m}^{\mathbf{s}}}{\tau_{\mathbf{c}}^{\mathbf{s}}+\tau_{\mathbf{bs}}^{\mathbf{s}}}\right)^{\mathbf{2N-1}}\frac{\mathbf{1}}{\tau_{\mathbf{c}}^{\mathbf{s}}+\tau_{\mathbf{bs}}^{\mathbf{s}}}\mathbf{m}^{\mathbf{s}}\right|}\left(\frac{\boldsymbol{\sigma}^{c}\cdot\mathbf{m}^{s}}{\tau_c^s+\tau_{bs}^s}\right)^{2\mathrm{N}-1}\frac{1}{\tau_c^s+\tau_{bs}^s}. \tag{49}$$

The semi-implicit integration procedure is applied to define the constitutive relation (Dunne and Petrinic, 2005). Details of the integration procedure are given in appendix B. The linearized form of single crystal constitutive law consistent with the integration procedure is:

$$\Delta\boldsymbol{\sigma}^c = \frac{\partial\Delta\boldsymbol{\sigma}^c}{\partial\Delta\varepsilon^c}\Delta\varepsilon^c + \Delta\boldsymbol{\sigma}^{c,*} = \frac{\partial\Delta\boldsymbol{\sigma}^c}{\partial\Delta\varepsilon^c}(\Delta\varepsilon^c - \Delta\varepsilon^{c,*}). \tag{50}$$

where $\Delta\varepsilon^{c,*}$ is calculated by replacing $\Delta\boldsymbol{\sigma}^c = \mathbf{C}^c(\Delta\varepsilon^c - \Delta\Lambda\hat{\mathbf{n}})$ in Eq. (50):

$$\Delta\varepsilon^{c,*} = \Delta\varepsilon^c - \frac{\partial\Delta\boldsymbol{\sigma}^c}{\partial\Delta\varepsilon^c}^{-1}\mathbf{C}^c(\Delta\varepsilon^c - \Delta\Lambda\hat{\mathbf{n}}). \tag{51}$$

The homogenization procedure for the linearized response of non-linear constituents is known as the affine formulation with step-wise reference to a linear comparison medium with an eigenstrain, for each grain and for the overall behavior (Masson et al., 2000). The details are presented in appendix C.

The idea behind regularized Schmid law is the introduction of the dependence between slip systems, controlled with the exponent *N*. Therefore, all slip systems are always active and shear rates between slip systems are connected i.e. shear rate and appearance of slip depends on shear stress on all slip systems. The introduced concept is different from the standard Schmid law which assumes independence between slip systems. In this sense the idea of regularized Schmid law is opposite to the one of diagonalization procedure i.e. regularized Schmid law introduces the dependence between slip systems, while diagonalization procedure is removing the dependence between slip systems.

To validate the single crystal integration procedure, a number of strain increments ($\Delta\varepsilon_{11} = 1e - 5$, $\Delta\varepsilon_{22} = -0.5e - 5$, $\Delta\varepsilon_{33} = -0.5e - 5$, $\Delta\varepsilon_{12} = \Delta\varepsilon_{13} = \Delta\varepsilon_{23} = 0$) are applied to an arbitrary crystal of the following crystal orientation (23,12,308). It is worth mentioning that the amount of strain per increment needs to be sufficiently small to avoid any numerical issues, since the semi-implicit algorithm is employed and the equations can be very stiff if *N* is large (Knezevic et al., 2016b). The initial slip resistance is set to 50 MPa and the hardening is defined using Eq. (41) with $h_r = 0$. Fig. 5 compares predictions from the regularized Schmid law and

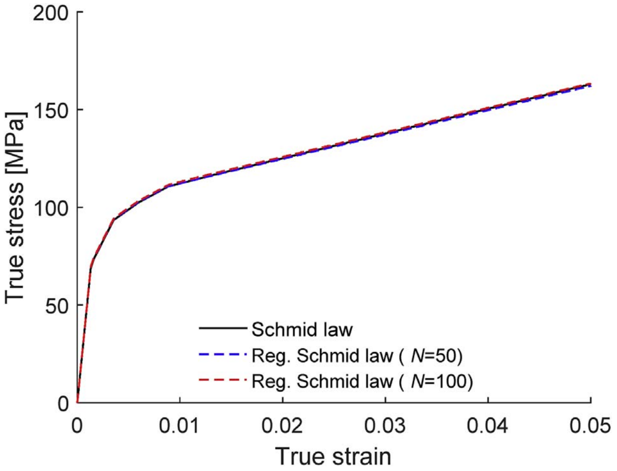

Fig. 5. Comparison of mechanical response for a single crystal deformed by imposing strain increments ($\Delta\varepsilon_{11} = 1e - 5$, $\Delta\varepsilon_{22} = -0.5e - 5$, $\Delta\varepsilon_{33} = -0.5e - 5$, $\Delta\varepsilon_{12} = \Delta\varepsilon_{13} = \Delta\varepsilon_{23} = 0$) for Schmid law and the regularized Schmid law. Two different values of the power-law parameters *N* are used, which controls the sharpness of the corners of single crystal yield surfaces.

the usual Schmid law. Evidently, the predictions are identical, validating the implementation of the regularized Schmid law procedure. In addition, the regularized Schmid law predictions with both $N = 50$ and $N = 100$ give similar results. Increasing the exponent N improves the accuracy at the yield surface corners but also increases the computational time.

3.6.3. A case study comparing the procedures for overcoming the singularity in the Eshelby tensor calculation: simple tension of AA6022-T4

In this section, a comparison is made between the standard EPSC and two approaches for overcoming the numerical loss of ellipticity: (1) diagonalization of the hardening matrix procedure and (2) regularized Schmid law procedure. The goals are to quantify their deviation from the standard EPSC by comparing predicted mechanical responses and to choose a more suitable method for predicting the anisotropy of AA6022-T4. The comparison is performed on the same set of 200 grains sampled from the ODF in Fig. 2c. For simplicity, texture evolution is turned off for the simulations presented in this section, while texture evolution is enabled in all other simulations presented in the following sections. The constant hardening matrix used for theory 1 formulation is:

$$h^{ss'} = \begin{cases} hc & \text{if } s = s' \\ 0.95 \times hc & \text{if } s \neq s' \end{cases}. \tag{52}$$

where $hc = 150\text{ MPa}$ is the chosen hardening rate. Simple tension along the RD is simulated. The same simulation is also performed while using the diagonalization of the hardening matrix and the regularized Schmid law procedures. Since these schemes alter the mechanical response for a given hardening matrix, Eq. (52), the constant hardening rate, hc, was adjusted such that the three simulations provide approximately the same true stress-true strain response in tension: 126 MPa when $r = 0$, 141.5 MPa when $r = 0.95$, and 122 MPa for the regularized Schimd law simulations. We remind that for $r = 1$, the standard EPSC formulation is retrieved. The initial slip resistance was kept at 50 MPa for simulations with the diagonalization of hardening matrix and standard EPSC, while it was set to 47 MPa for the simulation with the regularized Schmid law. Fig. 6a shows the comparison of simulation results, indicating that the mechanical response of all simulations is essentially identical. Fig. 6b shows that the predictions of r-ratio are also similar for all simulations. Fig. 6c, d, and e show the deviation of microscopic from macroscopic quantities. The compared quantities are tangent stiffness, strain, and stress rates. In the first case, the difference between single crystal tangent stiffness tensors and the overall macroscopic stiffness is calculated for each crystal using $d^c(\mathbf{L}, \mathbf{L}^c) = \frac{2\mathbf{L} - \mathbf{L}^c}{\mathbf{L} + \mathbf{L}^c}$ and the volume average is then calculated. It can be seen that methods for overcoming the loss of ellipticity result in a lower mean deviation relative to the standard EPSC, meaning that single crystal tangent stiffness tensors are more similar among different crystal orientations. The deviation of single crystal strain rate and stress rate is calculated using $\frac{\| \sqrt{(\dot{\varepsilon} - \dot{\varepsilon}^c)^2} \|}{\| \dot{\varepsilon} \|}$ and $\frac{\| \sqrt{(\dot{\sigma} - \dot{\sigma}^c)^2} \|}{\| \dot{\sigma} \|}$ and plotted in Fig. 6d and e, respectively, after performing volume averaging. The plot shows that single crystal strain rate varies less from the macroscopic strain rate for the methods introduced to overcome the loss of ellipticity than that for the standard EPSC. However, the regularized Schmid law predicts the most similar strain rates amongst grains, resembling the Taylor iso-strain homogenization assumption, which was also noted in (Yoshida et al., 2009). The stress rate deviation behaves in the opposite manner to strain rate deviation. As expected, the diagonalization of hardening matrix with the diagonalization parameter of $r = 0.95$ predicts the response which is the closest to the standard EPSC.

From the analysis presented in this section we conclude that the diagonalization of hardening matrix gives results more similar to the standard EPSC than the regularization of Schmid law. The regularized Schmid law procedure served as a reference for comparing the developed hardening matrix diagonalization procedure, but in itself is very computationally involved, especially for $N > 50$, since it has the semi-implicit integration algorithm. The new procedure developed herein for overcoming the loss of ellipticity enabled the use of experimentally determined latent hardening constants. It should be noted that the diagonalization of hardening with $r = 0$ matrix procedure gives diagonal hardening matrix for active slip systems, conforming to theory 2 latent hardening (Bassani and Wu, 1991a; Cuitino and Ortiz, 1993; Wu et al., 1991a). The developed procedure with EPSC is used in the subsequent sections for predicting the anisotropy of AA6022-T4 alloy.

4. Results and discussion

4.1. Predictions using the standard EPSC model

We begin by presenting the predictions using the model without the modifications pertaining to the hardening (Zecevic and Knezevic, 2015). Hardening along with latent hardening and backstress parameters are calibrated towards the data in Fig. 2. We emphasize that the crystallographic texture is mainly governing the anisotropy in this case.

The simple tension simulations are performed by enforcing increments in strain in a given direction of tension, while keeping the lateral stresses and shear strains at zero. The three measured stress-strain curves were used for fitting the hardening law parameters, while simulation results for r-ratio are considered as predictions. Table 1 shows the best fit parameters established for AA6022-T4. Theory 1 of latent hardening was used with the self-hardening coefficients set to unity ($L^{ss} = 1$) and the latent hardening coefficients set to 0.99 ($L^{ss'} = 0.99$ with $s \neq s'$), since the magnitude for the latter coefficients of 1 or greater causes loss of ellipticity for single crystals. As discussed, the use of more realistic (experimentally established) latent hardening coefficients is not possible within the standard EPSC implementation due to convergence issues. The starting measured texture shown in Fig. 2b was used to generate an input orientation distribution function (ODF) with MTEX matlab tool box (Bachmann et al., 2010), where 2000 weighted orientations were appropriately sampled and used as the starting texture for simulations. The invariant single crystal elastic constants for Al are: $C_{11} = 108.2\text{ GPa}$, $C_{12} = 61.3\text{ GPa}$, and $C_{44} = 28.5\text{ GPa}$ (Meyers and Chawla, 2009).

Fig. 7 shows the predictions in terms of true stress-true strain response and r-ratio. Evidently, the anisotropy in the mechanical

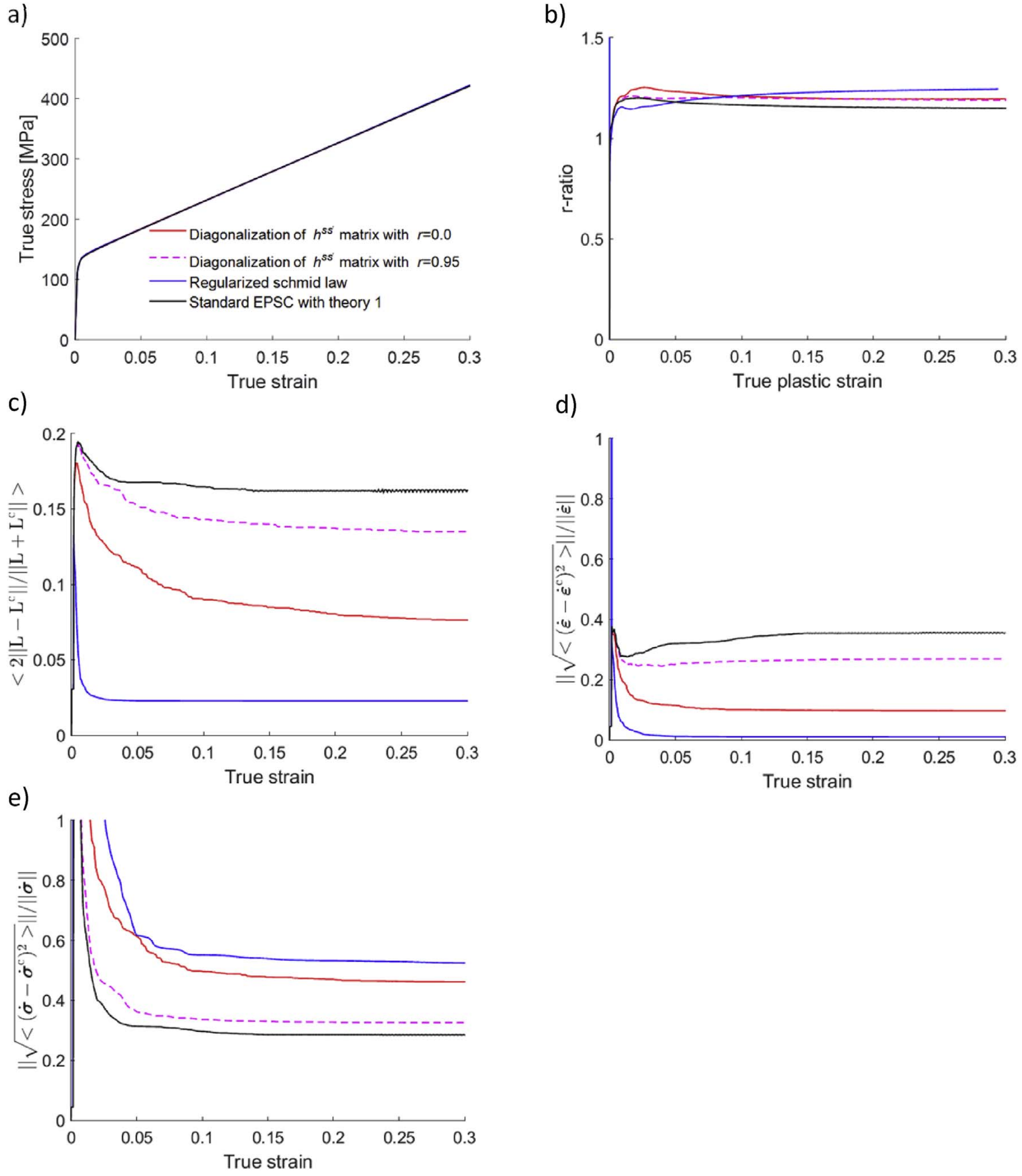

Fig. 6. Comparison of: (a) true stress-true strain curves, (b) r-ratio, (c) volume average of the difference between single crystal and macroscopic tangent stiffness, (d) the volume average difference between single crystal strain rate and applied strain rate and (e) the volume average difference between single crystal stress rate and applied stress rate, calculated by models indicated in the legend.

Table 1a
Constitutive parameters for the evolution of slip resistance for {111}<1$\bar{1}$0> slip mode in AA6022-T4.

τ_0 [MPa]	k_1 [m^{-1}]	g	D [MPa]	q
60	1.4×10^8	0.0784	100	16

Table 1b
Parameters for the evolution of slip system kinematic backstress in AA6022-T4.

τ_{bs}^{sat} [MPa]	ν	γ_b	A
5	560	0.001	10

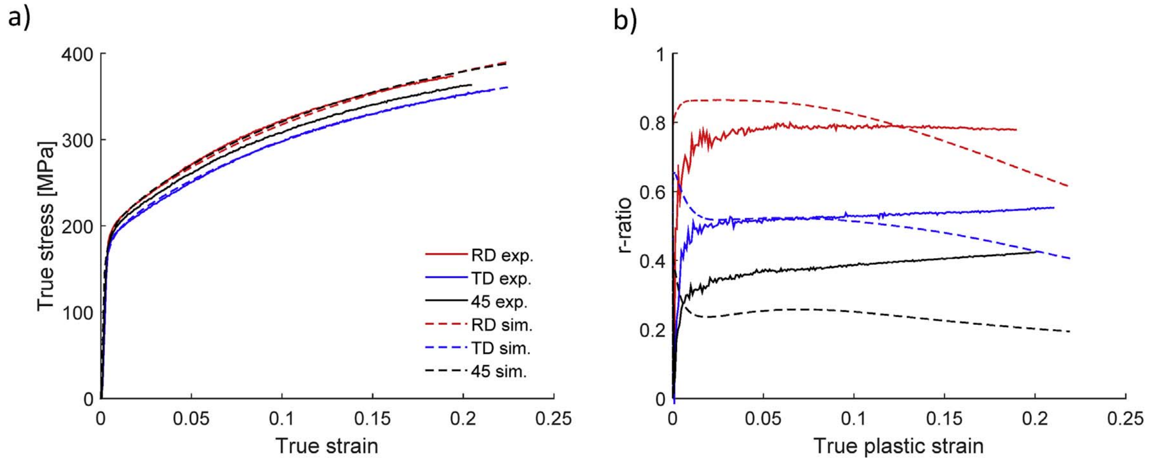

Fig. 7. Comparison of predictions using the standard EPSC and measurements for AA6022-T4: (a) true stress-true strain response and (b) r-ratio.

response is not well predicted. Note that lateral strain components (those in 22 and 33 directions if the loading is in 11 direction), which determine the r-ratio, are calculated from a system of linear equations given with Eq. (12). The system is solved using known values of strain rate and Jaumann stress rate, which are based on imposed boundary conditions. The solution for the system of linear equations in terms of the unknown strain rates in the directions 22 and 33 is in function of L_{21}, L_{22}, L_{23}, L_{31}, L_{32} and L_{33} components of the polycrystal tangent stiffness tensor of HEM. The homogenous effective medium is a fictitious homogenous material that behaves in the same way as the heterogeneous polycrystal. The tangent stiffness of the HEM is dependent on the selected homogenization approach, single crystal tangent stiffness, and texture. The single crystal tangent stiffness depends on the adopted hardening law. Therefore, the hardening law integrating the latent hardening and texture evolution govern the r-ratio evolution within the self-consistent homogenization approach used here. Thus, in our model, the predicted r-ratio is a direct consequence of the evolution of the polycrystal tangent stiffness, originating in the hardening rate and texture.

Next, we present results in terms of predicted plastic anisotropy of AA6022-T4 using EPSC formulation with the diagonalization of the hardening matrix procedure and the singular value decomposition for solving for single crystal stress increment. Predictions of mechanical response will allow us to discuss the origin of plastic anisotropy in the material.

4.2. *Predictions based on the strength interaction matrix $L^{ss'}$*

The strength interaction matrix in Eq. (18) is defined to contain six independent coefficients aimed at describing six types of dislocation interactions. The possible dislocation interactions are: (1) self-interaction between dislocations belonging to the same slip system, (2) coplanar-interaction between dislocations on the same slip plane, (3) interaction resulting in Hirth lock, (4) collinear interaction between dislocations on cross slip planes, (5) interaction resulting in sessile Lomer-Cottrell locks, and (6) glissile lock. However, a recent study involving latent hardening models utilizing up to six interaction coefficients revealed that the simplified strength interaction matrix of two entries were sufficiently general to predict anisotropy in FCC metals (Khadyko et al., 2016). Here, we assumed the self-hardening and the coplanar interactions as unity, while the other interactions were set to 1.4 consistent with the measurements performed on Al single crystals in (Kocks and Brown, 1966). Thus, the interaction matrix is reduced to two independent coefficients, governing the self and latent hardening. Several earlier studies made the same assumption (Anand and Kothari, 1996; Asaro and Needleman, 1985; Peirce et al., 1982). The fitted hardening law parameters are given in Table 2. The interaction matrix used in the evolution law for dislocation density (Eqs. (21)–(23)) is $g^{ss} = 1$ and $g^{ss'} = 0$ with $s \neq s'$. The fitted parameters for backstress are given in Table 1b.

Table 2
Constitutive parameters for the evolution of slip resistance for {111}<1$\bar{1}$0> slip mode in AA6022-T4.

τ_0 [MPa]	$k_1\,[m^{-1}]$	g	D [MPa]	q
56	1.3×10^8	0.0618	100	8

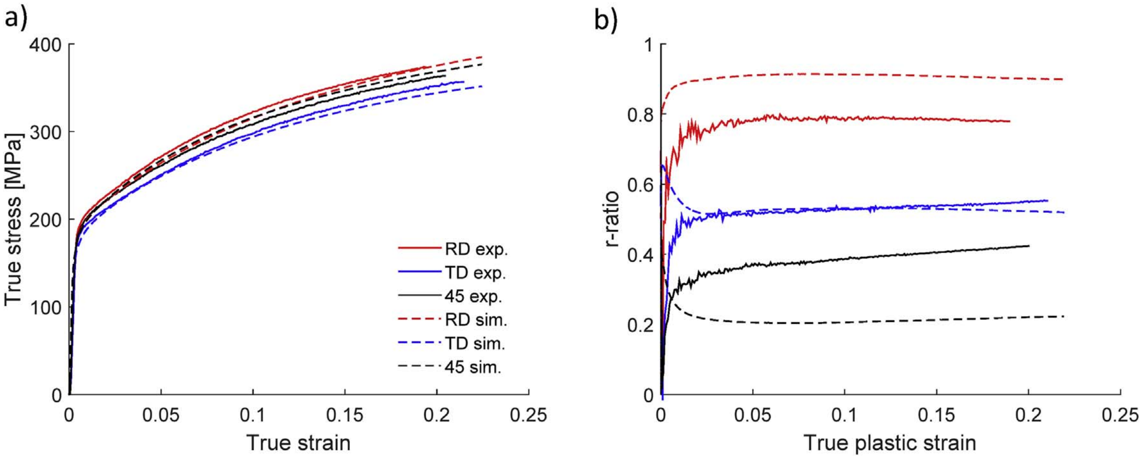

Fig. 8. Comparison of the predictions and measurements for AA6022-T4: (a) true stress-true strain response and (b) r-ratio.

The results are shown in Fig. 8. The simulated stress-strain curves to larger plastic strains follow the same trend as measured curves. However, the 45 direction stress is slightly over-predicted, while the TD direction stress is slightly under-predicted. The predictions of r-ratio follow similar trends as measurements, while the actual values are not matching very well needing further investigation. We note that the r-ratio predictions are not affected by the strength interaction matrices. Nevertheless, with the diagonalization of hardening matrix procedure, we no longer observe the decreasing r-ratio with plastic strain, which is a significant improvement.

To highlight the effect of latent hardening on plastic anisotropy in the flow curves of AA6022-T4, several simulations were run with the self-hardening ($L^{ss'}$) set to 1.0, while the latent hardening ($L^{ss'}$ with $s \neq s'$) was varied between 0 and 2. In all these simulation cases, the diagonalization of the hardening matrix $\boldsymbol{r} = 0$ method was used. Additionally, the predictions of the standard EPSC are also presented for the purpose of comparison. The dislocation-based hardening law parameters were slightly adjusted for each simulation case. The parameters are given in Table 3. The backstress parameters were kept the same, as presented in Table 1b. Fig. 9 compares the experimental and simulated ratio of the true stress in tensile direction for the three studied directions to the true stress in tension along the RD sample at a true strain of 0.18. It can be seen that the flow stress ratio for 45° and TD is decreasing with the latent hardening coefficients. Anisotropy in flaw stress follows the experimental trend ($\sigma_{RD} > \sigma_{45} > \sigma_{TD}$) better when the latent hardening coefficient is ≥ 1. In addition, Fig. 9 shows the effect of diagonalization of hardening matrix on anisotropy. The effect can be appreciated by focusing on the predictions from the standard EPSC and the predictions from the diagonalization of the hardening matrix for constants $L^{ss'}= 0.99$ and $L^{ss} = 1$. The comparison reveals that even with similar latent hardening, the diagonalization of hardening matrix produces the desired trend in the flow stress anisotropy. Evidently, the experimental values adopted from (Kocks and Brown, 1966) further improve the predictions.

4.3. Improved predictions using the interaction matrix $g^{ss'}$

The predictions presented thus far considered $g^{ss'}$ as diagonal matrix populated with the values of unity on the diagonal. The rate of dislocation generation per slip system is dependent on dislocation density in itself and other slip systems in a complex manner (Kubin et al., 2008a). In the dislocation evolution law, the interdependence between slip systems in terms of generation of dislocations can be implemented by increasing the off-diagonal terms in $g^{ss'}$. The $g^{ss'}$ controls the dislocation evolution rate in the same way the $L^{ss'}$ controls the slip resistance. The hardening rate of a slip system, defined with entries of hardening matrix in appendix A, is proportional to dislocation evolution rate. Therefore, the rate of hardening of all slip systems due to shearing on an active slip system is controlled in part by $g^{ss'}$ interaction matrix. The strength interaction matrix, $L^{ss'}$, remained the same, i.e. the self-hardening and the coplanar interactions are unity while all the remaining terms are 1.4. The effect of increasing off-diagonal terms in matrix $g^{ss'}$ on anisotropy in flow stress is shown in Fig. 10a. The predictions improve with increasing the magnitude of the $g^{ss'}$ off-diagonal entries but then saturate. No appreciable improvements are obtained after a value of 1 for the off-diagonal entries. The empirical backstress

Table 3
Constitutive parameters for the evolution of slip resistance for {111}<1$\bar{1}$0> slip mode in AA6022-T4.

L^{ss}	$L^{ss'}$	g^{ss}	$g^{ss'}$	τ_0 [MPa]	$k_1\,[m^{-1}]$	g	D [MPa]	q
1	0	1	0	60	3.0×10^8	0.1176	100	8
1	0.5	1	0	60	1.6×10^8	0.0866	100	8
1	1	1	0	58	1.3×10^8	0.0706	100	8
1	2	1	0	56	1.1×10^8	0.0523	100	8

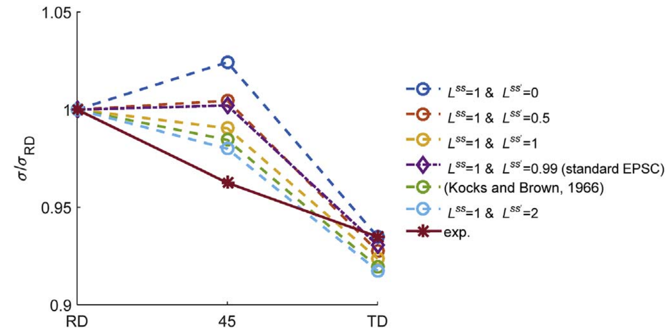

Fig. 9. True stress at a true strain of 0.18 predicted in tension along the three directions as indicated on the x-axis normalized by the tensile true stress in RD. The corresponding experimental results are presented to facilitate the comparison.

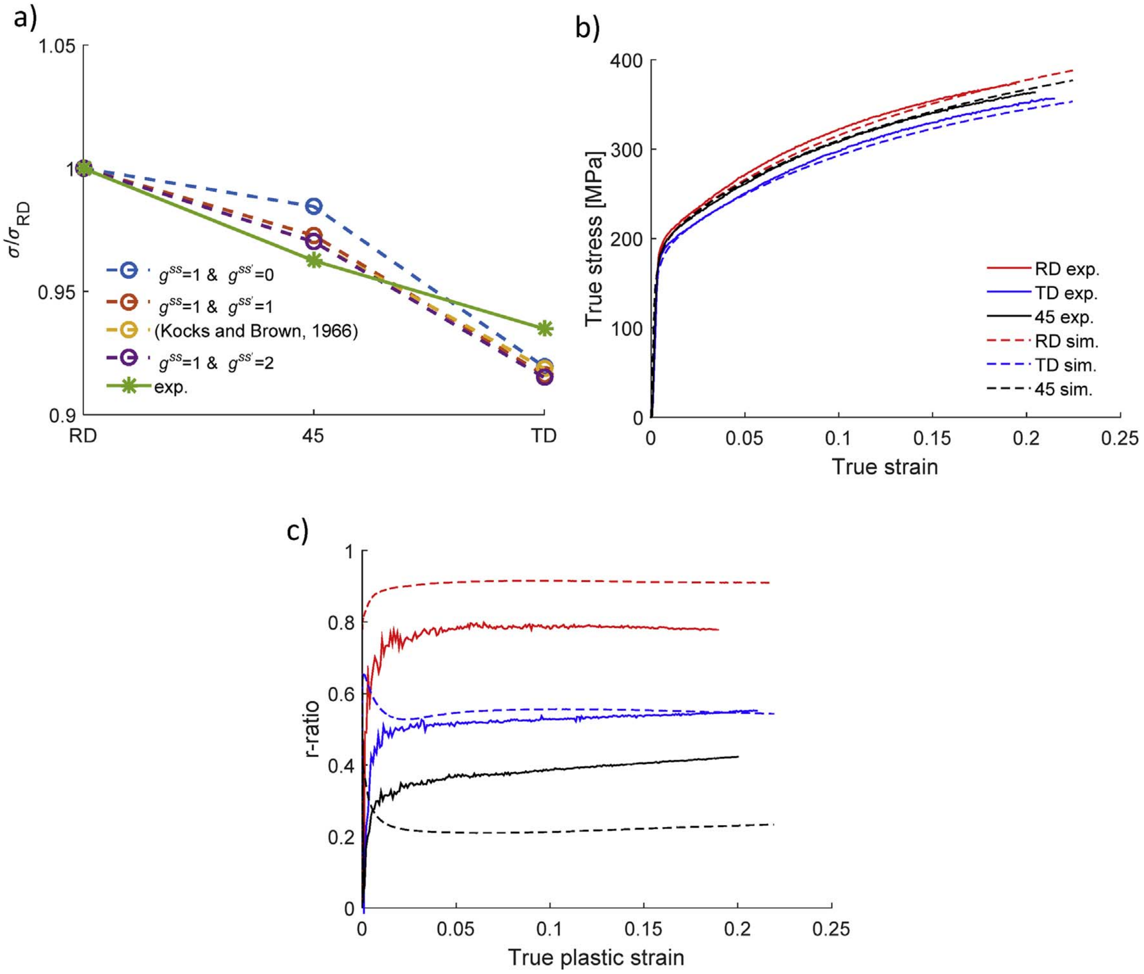

Fig. 10. (a) True stress at a true strain of 0.18 predicted in tension along the three directions as indicated on the x-axis normalized by the tensile true stress in RD. The corresponding experimental results are presented to facilitate the comparison. (a) Comparison of simulated and measured true stress-true strain curves and (b) simulated and measured r-ratio for AA6022-T4.

law is still used with the parameters given in Table 1b. As always, the hardening law parameters were adjusted to obtain the best fit to the measured data and are given in Table 4. The fits to true stress-true strain curves and the predictions of r-ratio are given in Fig. 10b and c, respectively. Evidently, the model successfully captures the evolution of anisotropy. We regard the predicted trends as good. We note that introducing the off-diagonal terms in the matrix $g^{ss'}$ within the standard EPSC can have some positive effect on the flow stress anisotropy, while the r-ratio predictions become worse.

In summary, the simulation results reveal that the strength interaction matrix, $L^{ss'}$, and the interaction matrix defining the rate of

Table 4
Constitutive parameters for the evolution of slip resistance for {111}<1$\bar{1}$0> slip mode in AA6022-T4. The (Kocks and Brown, 1966) refers to setting self and coplanar interactions between slip systems to 1.0, while all other interactions are defined to be 1.4.

L^{ss}	$L^{ss'}$	g^{ss}	$g^{ss'}$	τ_0 [MPa]	k_1 [m^{-1}]	g	D [MPa]	q
(Kocks and Brown, 1966)		1	0	56	1.3×10^8	0.0618	100	8
		1	1	56	0.65×10^8	0.0294	100	8
		(Kocks and Brown, 1966)		56	0.65×10^8	0.0244	100	8
		1	2	56	0.5×10^8	0.022	100	8

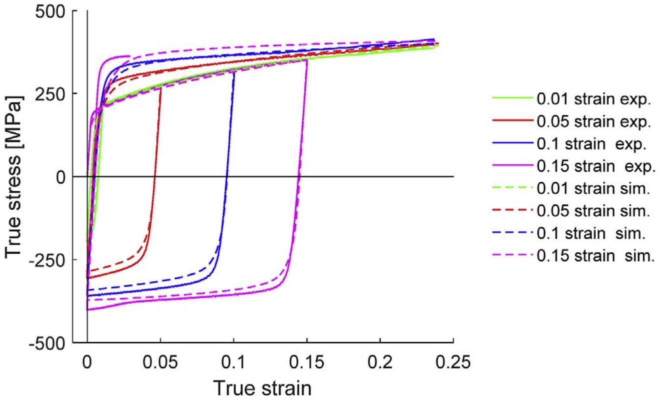

Fig. 11. Comparison of measured (solid lines) and predicted (dashed lines) large strain cyclic tension-compression response along RD. The predictions are based on the new EPSC model with diagonalization of hardening matrix.

dislocation generation, $g^{ss'}$, for the given crystallographic texture and its evolution have a significant effect on the observed anisotropy in stress-strain response of AA6022-T4.

4.4. Large strain cyclic plasticity predictions for AA6022-T4

Finally, the predictive characteristics of the model are evaluated on the large strain cyclic data for the material. The presented dislocation density-based hardening along with the empirical backstress model with the parameters given in Tables 4 and 1b has been utilized in the EPSC model with the diagonalization of the hardening matrix procedure for these calculations. The reversibility parameter was set to $p = 0.2$ (Eqs. (21)–(23)). Fig. 11 shows the predictions. It can be seen that the model using the single set of parameters is capable of predicting the non-linear unloading, the BE, and the hardening rates upon loading in the reverse direction of the material with reasonable accuracy. Therefore, the EPSC integrating the diagonalization of the hardening matrix is able to produce similar predictions of the cyclic response to those of the standard EPSC (Zecevic and Knezevic, 2015).

5. Conclusions

This paper extends a recently developed dislocation-based hardening law within the EPSC homogenization (Zecevic and Knezevic, 2015; Zecevic et al., 2016a) to incorporate the latent hardening effects for the prediction of plastic anisotropy of polycrystalline metals. The new implementation overcomes an issue in the self-consistent formulation with latent hardening arising when experimentally measured latent hardening constants are used. The main issue is identified to be the loss of ellipticity of macroscopic tangent modulus caused by the loss of ellipticity of single crystal tangent modulus. The new method takes the advantage of a new solution procedure for single crystal stress increment relying on the singular value decomposition to solve for shear increments. The method, termed the diagonalization of hardening matrix, is compared with the regularized Schmid law method, which does not have the issue with the loss of ellipticity. The comparison shows that the new implementation is closer in terms of stress-strain predictions to the original EPSC formulation than the regularized Schmid law, leading to more accurate predictions. Moreover, the new method is much more computationally efficient.

Effect of latent hardening on plastic anisotropy in the mechanical response of AA6022-T4 is studied using the developed crystallographic modeling framework. The proposed method for overcoming the loss of ellipticity, which facilitates the use of the experimentally determined latent hardening coefficients for aluminum reported in (Kocks and Brown, 1966), predicts the correct anisotropy in the stress-strain response of the studied material. Thus, the latent hardening, along with crystallographic texture evolution, are found to control plastic anisotropy in AA6022-T4. Moreover, the model improves the predictions of r-ratio evolution with plastic strain. Finally, the proposed model is able to predict the large strain cyclic plasticity behavior of the material.

Acknowledgments

This work is based upon projects supported by the US National Science Foundation under grants CMMI-1301081 and CMMI-1650641.

Appendix A

Entries of the hardening matrix are partial derivatives of slip resistance given with relation (17) with respect to shear strain on slip systems:

$$h^{ss'} = \frac{\partial \tau_c^s}{\partial \gamma^{s'}} = \frac{\partial \tau_0^\alpha}{\partial \gamma^{s'}} + \frac{\partial \tau_{forest}^s}{\partial \gamma^{s'}} + \frac{\partial \tau_{debris}^\alpha}{\partial \gamma^{s'}}. \tag{A1}$$

The index s' goes over all active slip systems. Since the initial slip resistance, τ_0^α, is a constant its derivative vanish, while derivatives of the forest and debris contributions to slip resistance are:

$$\frac{\partial \tau_{forest}^s}{\partial \gamma^{s'}} = \frac{\partial \tau_{forest}^s}{\partial \rho_{tot}^{s'}} \frac{\partial \rho_{tot}^{s'}}{\partial \gamma^{s'}} = b^\alpha \chi \mu^\alpha \frac{1}{2\sqrt{\sum_{s'} L^{ss'} \rho_{tot}^{s'}}} L^{ss'} \left(\frac{\partial \rho_{for}^{s'}}{\partial \gamma^{s'}} + \frac{\partial \rho_{rev}^{s'+}}{\partial \gamma^{s'}} + \frac{\partial \rho_{rev}^{s'-}}{\partial \gamma^{s'}} \right), \tag{A2}$$

$$\frac{\partial \tau_{debris}^\alpha}{\partial \gamma^{s'}} = \frac{\partial \tau_{debris}^\alpha}{\partial \rho_{deb}} \frac{\partial \rho_{deb}}{\partial \gamma^{s'}} = -k_{deb} \mu^\alpha b^\alpha (log\,(b^\alpha \sqrt{\rho_{deb}}) + 1) \frac{1}{2\sqrt{\rho_{deb}}} \frac{\partial \rho_{deb}}{\partial \gamma^{s'}}. \tag{A3}$$

The derivatives of forward, reversible, and debris dislocation densities with respect to shear strain are provided with Eqs. (21a-23b, 26) respectively.

Similarly, entries of the backstress matrix are partial derivatives of backstress given with relation (27) with respect to shear strain on slip systems:

$$h_{bs}^{ss'} = \frac{\partial \tau_{bs}^s}{\partial \gamma^{s'}} = \begin{cases} \frac{\partial \tau_{bs,sys}^s}{\partial \gamma^s} & if\ s = s' \\ 2\, \mathbf{m}^s \cdot \mathbf{m}^{s'} \frac{\partial \tau_{bs,sys*}^{s'}}{\partial \gamma^{s'}} & if\ s \neq s' \end{cases} \tag{A4}$$

where s' goes over set of active slip systems. Using the relation (28) the derivative $\frac{\partial \tau_{bs,sys*}^{s'}}{\partial \gamma^{s'}}$ is:

$$\frac{\partial \tau_{bs,sys*}^{s'}}{\partial \gamma^{s'}} = \begin{cases} \frac{\partial \tau_{bs,sys}^{s'}}{\partial \gamma^{s'}} & if\ \tau_{bs,sys}^{s'} > 0 \\ 0 & if\ \tau_{bs,sys}^{s'} < 0 \end{cases} \tag{A5}$$

Next we define the derivative of slip system backstress sources, $\frac{\partial \tau_{bs,sys}^s}{\partial \gamma^s}$. In the case of shearing in s^+ direction, $d\gamma^{s^+} > 0$, with $\tau_{bs}^{s^+} \geq 0$:

$$\frac{\partial \tau_{bs,sys}^{s^+}}{\partial \gamma^{s^+}} = \tau_{bs}^{sat} \nu \exp\left(-\nu \gamma^{s^+}\right), \tag{A6}$$

$$\frac{\partial \tau_{bs,sys}^{s^-}}{\partial \gamma^{s^+}} = -A \frac{\partial \tau_{bs,sys}^{s^+}}{\partial \gamma^{s^+}}. \tag{A7}$$

The derivative of slip system backstress source in case of shearing in s^+ direction, $d\gamma^{s^+} > 0$, with $\tau_{bs,sys}^{s^+} < 0$ is:

$$\frac{\partial \tau_{bs,sys}^{s^+}}{\partial \gamma^{s^+}} = \frac{(A+1)\tau_{bs}^{sat}}{\gamma_b} \exp\left(-\frac{\gamma^{s^+}}{\gamma_b}\right), \tag{A8}$$

$$\frac{\partial \tau_{bs,sys}^{s^-}}{\partial \gamma^{s^+}} = -\frac{1}{A} \frac{\partial \tau_{bs,sys}^{s^+}}{\partial \gamma^{s^+}}. \tag{A9}$$

Appendix B

The purpose of integration algorithm is to find an increment in plastic multiplier $\Delta\Lambda$, for a given increment in a crystal strain, $\Delta\varepsilon^c$. In the semi-implicit integration procedure (Dunne and Petrinic, 2005) the normal to yield surface is evaluated at the beginning of the time increment by calculating:

$$\hat{\mathbf{n}}_t = \frac{1}{\left|\sum_{\mathbf{s}}\left(\frac{\boldsymbol{\sigma}^{\mathbf{c}}_{\mathbf{t}}\cdot\mathbf{m}^{\mathbf{s}}_{\mathbf{t}}}{\tau^{\mathbf{s}}_{\mathbf{c},\mathbf{t}}+\tau^{\mathbf{s}}_{\mathbf{bs},\mathbf{t}}}\right)^{\mathbf{2N-1}}\frac{\mathbf{1}}{\tau^{\mathbf{s}}_{\mathbf{c},\mathbf{t}}+\tau^{\mathbf{s}}_{\mathbf{bs},\mathbf{t}}}\mathbf{m}^{\mathbf{s}}_{\mathbf{t}}\right|}\sum_s\left(\frac{\boldsymbol{\sigma}^c_t\cdot\mathbf{m}^s_t}{\tau^s_{c,t}+\tau^s_{bs,t}}\right)^{2N-1}\frac{1}{\tau^s_{c,t}+\tau^s_{bs,t}}\mathbf{m}^s_t. \tag{B1}$$

All variables having subscript t are written at instant t and are known. Therefore, in Eq. (B1), all variables on the right hand side are known, and $\hat{\mathbf{n}}_t$ can simply be calculated. The yield function is written at the end of the time increment:

$$f_{t+\Delta t} = \left(\sum_s\left(\frac{\boldsymbol{\sigma}^c_{t+\Delta t}\cdot\mathbf{m}^s_t}{\tau^s_{c,t+\Delta t}+\tau^s_{bs,t+\Delta t}}\right)^{2N}\right)^{\frac{1}{2N}} - 1 = 0, \tag{B2}$$

with:

$$\boldsymbol{\sigma}^c_{t+\Delta t} = \boldsymbol{\sigma}^c_t + \Delta\boldsymbol{\sigma}^c = \boldsymbol{\sigma}^c_t + \mathbf{C}^c(\Delta\boldsymbol{\varepsilon}^c - \Delta\Lambda\hat{\mathbf{n}}_t), \tag{B3}$$

$$\tau^s_{c,t+\Delta t} = \tau^s_{c,t} + \sum_{s'} h^{ss'}_t\Delta\gamma^{s'} = \tau^s_{c,t} + \Delta\Lambda\sum_{s'} h^{ss'}_t\hat{n}^{s'}_t, \tag{B4}$$

$$\tau^s_{bs,t+\Delta t} = \tau^s_{bs,t} + \sum_{s'} h^{ss'}_{bs,t}\Delta\gamma^{s'} = \tau^s_{bs,t} + \Delta\Lambda\sum_{s'} h^{ss'}_{bs,t}\hat{n}^{s'}_t, \tag{B5}$$

where $\Delta\Lambda$ is the increment in plastic multiplier. (B2) is a non-linear equation with $\Delta\Lambda$ as unknown. Newton method is used to solve for $\Delta\Lambda$. Next, increments in shear strain on slip systems, slip resistance, plastic strain, and stress can be calculated and total variables updated.The consistent tangent operator is:

$$\frac{\partial\Delta\boldsymbol{\sigma}^c}{\partial\Delta\boldsymbol{\varepsilon}^c} = \frac{\partial}{\partial\Delta\boldsymbol{\varepsilon}^c}[\mathbf{C}^c(\Delta\boldsymbol{\varepsilon}^c - \Delta\Lambda\hat{\mathbf{n}})] = \mathbf{C}^c - \mathbf{C}^c\hat{\mathbf{n}}\otimes\frac{\partial\Delta\Lambda}{\partial\Delta\boldsymbol{\varepsilon}^c}, \tag{B6}$$

$\frac{\partial\Delta\Lambda}{\partial\Delta\boldsymbol{\varepsilon}^c}$ can be calculated by taking the derivative of relation (B2):

$$\begin{aligned}\frac{1}{2N}&\left(\sum_s\left(\frac{\boldsymbol{\sigma}^c_{t+\Delta t}\cdot\mathbf{m}^s_t}{\tau^s_{c,t+\Delta t}+\tau^s_{bs,t+\Delta t}}\right)^{2N}\right)^{\frac{1}{2N}-1} 2N\sum_s\left(\frac{\boldsymbol{\sigma}^c_{t+\Delta t}\cdot\mathbf{m}^s_t}{\tau^s_{c,t+\Delta t}+\tau^s_{bs,t+\Delta t}}\right)^{2N-1}\left[\frac{1}{\tau^s_{c,t+\Delta t}+\tau^s_{bs,t+\Delta t}}\frac{\partial(\boldsymbol{\sigma}^c_{t+\Delta t}\cdot\mathbf{m}^s_t)}{\partial\Delta\boldsymbol{\varepsilon}^c}\right.\\ &\left.-\frac{\boldsymbol{\sigma}^c_{t+\Delta t}\cdot\mathbf{m}^s_t}{(\tau^s_{c,t+\Delta t}+\tau^s_{bs,t+\Delta t})^2}\frac{\partial(\tau^s_{c,t+\Delta t}+\tau^s_{bs,t+\Delta t})}{\partial\Delta\boldsymbol{\varepsilon}^c}\right] = 0,\end{aligned} \tag{B7}$$

where:

$$\frac{\partial(\boldsymbol{\sigma}^c_{t+\Delta t}\cdot\mathbf{m}^s_t)}{\partial\Delta\boldsymbol{\varepsilon}^c} = \mathbf{m}^s_t\mathbf{C}^c - \mathbf{m}^s_t\mathbf{C}^c\hat{\mathbf{n}}_t\otimes\frac{\partial\Delta\Lambda}{\partial\Delta\boldsymbol{\varepsilon}^c}, \tag{B8}$$

$$\frac{\partial(\tau^s_{c,t+\Delta t}+\tau^s_{bs,t+\Delta t})}{\partial\Delta\boldsymbol{\varepsilon}^c} = \frac{\partial\Delta\Lambda}{\partial\Delta\boldsymbol{\varepsilon}^c}\sum_{s'}\left(h^{ss'}_t + h^{ss'}_{bs,t}\right)\hat{n}^{s'}_t. \tag{B9}$$

From (B7), $\frac{\partial\Delta\Lambda}{\partial\Delta\boldsymbol{\varepsilon}^c}$ can be expressed as:

$$\begin{aligned}\frac{\partial\Delta\Lambda}{\partial\Delta\boldsymbol{\varepsilon}^c}\\ &= \left(\sum_s\left(\frac{\boldsymbol{\sigma}^c_{t+\Delta t}\cdot\mathbf{m}^s_t}{\tau^s_{c,t+\Delta t}+\tau^s_{bs,t+\Delta t}}\right)^{2N-1}\frac{1}{\tau^s_{c,t+\Delta t}+\tau^s_{bs,t+\Delta t}}\mathbf{m}^s_t\mathbf{C}^c\right)\\ &\quad\left(\sum_s\left(\frac{\boldsymbol{\sigma}^c_{t+\Delta t}\cdot\mathbf{m}^s_t}{\tau^s_{c,t+\Delta t}+\tau^s_{bs,t+\Delta t}}\right)^{2N-1}\frac{1}{\tau^s_{c,t+\Delta t}+\tau^s_{bs,t+\Delta t}}\left(\mathbf{m}^s_t\mathbf{C}^c\hat{\mathbf{n}}_t + \frac{\boldsymbol{\sigma}^c_{t+\Delta t}\cdot\mathbf{m}^s_t}{\tau^s_{c,t+\Delta t}+\tau^s_{bs,t+\Delta t}}\sum_{s'}\left(h^{ss'}_t + h^{ss'}_{bs,t}\right)\hat{n}^{s'}_t\right)\right)^{-1}.\end{aligned} \tag{B10}$$

Appendix C

Constitutive relations in presence of eigenstrain for single crystal and polycrystal, respectively, are:

$$\Delta\boldsymbol{\sigma}^c = \mathbf{L}^c(\Delta\boldsymbol{\varepsilon}^c - \Delta\boldsymbol{\varepsilon}^{*c}), \tag{C1}$$

$$\Delta\boldsymbol{\sigma} = \mathbf{L}(\Delta\boldsymbol{\varepsilon} - \Delta\boldsymbol{\varepsilon}^*), \tag{C2}$$

where $\mathbf{L}^c = \frac{\partial\Delta\boldsymbol{\sigma}^c}{\partial\Delta\boldsymbol{\varepsilon}^c}$ is consistent tangent operator. Interaction equation for inhomogeneity inside the matrix is:

$$\Delta\boldsymbol{\sigma}^c - \Delta\boldsymbol{\sigma} = -\mathbf{L}^*(\Delta\boldsymbol{\varepsilon}^c - \Delta\boldsymbol{\varepsilon}), \tag{C3}$$

with $\mathbf{L}^* = \mathbf{L}((\mathbf{S}^{\mathbf{c}})^{-\mathbf{1}} - \mathbf{I})$. Replacing constitutive relation inside the interaction equation gives:

$$\mathbf{L}^c(\Delta\varepsilon^c - \Delta\varepsilon^{*c}) - \mathbf{L}(\Delta\varepsilon - \Delta\varepsilon^*) = -\mathbf{L}^*(\Delta\varepsilon^c - \Delta\varepsilon). \tag{C4}$$

From relation (C4) increment in strain can be expressed as:

$$\Delta\varepsilon^c = \mathbf{A}^c\Delta\varepsilon^{ref} + \mathbf{a}^c, \tag{C5}$$

with

$$\mathbf{A}^c = (\mathbf{L}^c + \mathbf{L}^*)^{-1}(\mathbf{L} + \mathbf{L}^*), \tag{C6}$$

$$\mathbf{a}^c = (\mathbf{L}^c + \mathbf{L}^*)^{-1}(\mathbf{L}^c\Delta\varepsilon^{*c} - \mathbf{L}\Delta\varepsilon^*), \tag{C7}$$

where $\Delta\varepsilon^{ref}$ is the unknown reference increment in strain (Lebensohn et al., 1996). Using the condition that the volume average of single crystal increments in strain is equal to the macroscopic increment in strain gives the expression for reference strain increment:

$$\Delta\varepsilon = \langle\boldsymbol{\Delta\varepsilon^c}\rangle = \langle\mathbf{A}^c\rangle\ \Delta\varepsilon^{ref} + \langle\mathbf{a}^c\rangle \rightarrow\ \Delta\varepsilon^{ref} = \langle\mathbf{A}^c\rangle^{-1}\Delta\varepsilon - \langle\mathbf{A}^c\rangle^{-1}\langle\mathbf{a}^c\rangle. \tag{C8}$$

In a similar manner, the volume average of single crystal increments in stress is equal to the macroscopic increment in stress:

$$\Delta\sigma = \langle\boldsymbol{\Delta\sigma^c}\rangle = \langle\mathbf{L}^c\mathbf{A}^c\rangle\langle\mathbf{A}^c\rangle^{-1}\Delta\varepsilon - \langle\mathbf{L}^c\mathbf{A}^c\rangle\langle\mathbf{A}^c\rangle^{-1}\langle\mathbf{a}^c\rangle + \langle\mathbf{L}^c(\mathbf{a}^c - \boldsymbol{\Delta\varepsilon^{*c}})\rangle. \tag{C9}$$

By comparing relation (C9) with (C2) we can identify macroscopic tangent stiffness and eigenstrain:

$$\mathbf{L} = \langle\mathbf{L}^c\mathbf{A}^c\rangle\langle\mathbf{A}^c\rangle^{-1}, \tag{C10}$$

$$\Delta\varepsilon^* = \langle\mathbf{a}^c\rangle - \mathbf{L}^{-1}\ \langle\mathbf{L}^c(\mathbf{a}^c - \Delta\varepsilon^{*c})\rangle. \tag{C11}$$

References

Al-Harbi, H.F., Knezevic, M., Kalidindi, S.R., 2010. Spectral approaches for the fast computation of yield surfaces and first-order plastic property closures for polycrystalline materials with cubic-triclinic textures. Comput. Mater. Continua (CMC): Comput. Mater. Continua (CMC) 15, 153–172.

Alcoa, Alloy 6022 Sheet, North American Rolled Products.

Anand, L., Kothari, M., 1996. A computational procedure for rate-independent crystal plasticity. J. Mech. Phys. Solid. 44, 525–558.

Anjabin, N., Karimi Taheri, A., Kim, H.S., 2014. Crystal plasticity modeling of the effect of precipitate states on the work hardening and plastic anisotropy in an Al–Mg–Si alloy. Comput. Mater. Sci. 83, 78–85.

Ardeljan, M., Beyerlein, I.J., Knezevic, M., 2014. A dislocation density based crystal plasticity finite element model: application to a two-phase polycrystalline HCP/BCC composites. J. Mech. Phys. Solids 66, 16–31.

Ardeljan, M., Beyerlein, I.J., Knezevic, M., 2017. Effect of dislocation density-twin interactions on twin growth in AZ31 as revealed by explicit crystal plasticity finite element modeling. Int. J. Plast. 99, 81–101.

Ardeljan, M., Beyerlein, I.J., McWilliams, B.A., Knezevic, M., 2016a. Strain rate and temperature sensitive multi-level crystal plasticity model for large plastic deformation behavior: application to AZ31 magnesium alloy. Int. J. Plast. 83, 90–109.

Ardeljan, M., Knezevic, M., Nizolek, T., Beyerlein, I.J., Mara, N.A., Pollock, T.M., 2015a. A study of microstructure-driven strain localizations in two-phase polycrystalline HCP/BCC composites using a multi-scale model. Int. J. Plast. 74, 35–57.

Ardeljan, M., McCabe, R.J., Beyerlein, I.J., Knezevic, M., 2015b. Explicit incorporation of deformation twins into crystal plasticity finite element models. Comput. Meth. Appl. Mech. Eng. 295, 396–413.

Ardeljan, M., Savage, D.J., Kumar, A., Beyerlein, I.J., Knezevic, M., 2016b. The plasticity of highly oriented nano-layered Zr/Nb composites. Acta Mater. 115, 189–203.

Asaro, R.J., Needleman, A., 1985. Texture development and strain hardening in rate dependent polycrystals. Acta Metall. Mater. 33, 923–953.

Bachmann, F., Hielscher, R., Schaeben, H., 2010. Texture analysis with MTEX - free and open source software Toolbox. Solid State Phenom. 160.

Barrett, T.J., Knezevic, M., Kuwabara, T., Hassan, T., Islam, N., Kinsey, B., Korkolis, Y., 2017. Continuous-banding-under Tension of AA6022-T4, Part 2. Analysis In preparation).

Bassani, J.L., Wu, T.-Y., 1991a. Latent hardening in single crystals II. Analytical characterization and predictions. Proc. Math. Phys. Sci. 435, 21–41.

Bassani, J.L., Wu, T.-Y., 1991b. Latent hardening in single crystals II. Analytical characterization and predictions. Proc. Royal Soc. Lond. A: Math., Phys. Eng. Sci. 435, 21–41.

Bauschinger, J., 1886. Über die Veränderung der Elasticitätsgrenze und Festigkeit des Eisen und Stahls durch Strecken und Quetschen, durch Erwarmen und Abkühlen und durch oftmal wiederholte Beanspruchung. Mitteilungen aus dem mechanisch-technischen Laboratorium der k. polytechnischen Schule 1877–1836.

Beaudoin, A.J., Dawson, P.R., Mathur, K.K., Kocks, U.F., Korzekwa, D.A., 1994. Application of polycrystal plasticity to sheet forming. Comput. Meth. Appl. Mech. Eng. 117, 49–70.

Ben Bettaieb, M., Débordes, O., Dogui, A., Duchêne, L., Keller, C., 2012. On the numerical integration of rate independent single crystal behavior at large strain. Int. J. Plast. 32–33, 184–217.

Beyerlein, I.J., Tomé, C.N., 2007. Modeling transients in the mechanical response of copper due to strain path changes. Int. J. Plast. 23, 640–664.

Beyerlein, I.J., Tomé, C.N., 2008. A dislocation-based constitutive law for pure Zr including temperature effects. Int. J. Plast. 24, 867–895.

Cuitino, A.M., Ortiz, M., 1993. Computational modelling of single crystals. Model. Simulat. Mater. Sci. Eng. 1, 225.

Devincre, B., Hoc, T., Kubin, L., 2008. Dislocation mean free paths and strain hardening of crystals. Science 320, 1745–1748.

Dunne, F., Petrinic, N., 2005. Introduction to Computational Plasticity. Oxford University Press.

Eghtesad, A., Zecevic, M., Lebensohn, R.A., McCabe, R.J., Knezevic, M., 2017. Spectral database constitutive representation within a spectral micromechanical solver for computationally efficient polycrystal plasticity modelling. Comput. Mech. https://doi.org/10.1007/s00466-017-1413-4.

Eshelby, J.D., 1957. The determination of the elastic field of an ellipsoidal inclusion, and related problems. Proc R. Soc. Lond. A 241, 376–396.

Franciosi, P., Berveiller, M., Zaoui, A., 1980. Latent hardening in copper and aluminium single crystals. Acta Metall. 28, 273–283.

Franciosi, P., Zaoui, A., 1982. Multislip in f.c.c. crystals a theoretical approach compared with experimental data. Acta Metall. 30, 1627–1637.

Franz, G., Abed-Meraim, F., Lorrain, J.-P., Ben Zineb, T., Lemoine, X., Berveiller, M., 2009. Ellipticity loss analysis for tangent moduli deduced from a large strain elastic–plastic self-consistent model. Int. J. Plast. 25, 205–238.

Freidin, A.B., Kucher, V.A., 2015. Solvability of the equivalent inclusion problem for an ellipsoidal inhomogeneity. Math. Mech. Solid 21, 255–262.

Fromm, B.S., Adams, B.L., Ahmadi, S., Knezevic, M., 2009. Grain size and orientation distributions: application to yielding of α-titanium. Acta Mater. 57, 2339–2348.

Gambin, W., 1992. Refined analysis of elastic-plastic crystals. Int. J. Solid Struct. 29, 2013–2021.

Golub, G.H., Loan, C.F.v., 1996. Matrix Computations. John Hopkins University Press, Baltimore MD.

Gupta, A.K., Lloyd, D.J., Court, S.A., 2001. Precipitation hardening in Al–Mg–Si alloys with and without excess Si. Mater. Sci. Eng. A 316, 11–17.

Harder, J., 1999. A crystallographic model for the study of local deformation processes in polycrystals. Int. J. Plast. 15, 605–624.
Hasegawa, T., Yakou, T., Karashima, S., 1975. Deformation behaviour and dislocation structures upon stress reversal in polycrystalline aluminium. Mater. Sci. Eng. 20, 267–276.
Hill, R., 1966. Generalized constitutive relations for incremental deformation of metal crystals by multislip. J. Mech. Phys. Solids 14, 95–102.
Hosford, W.F., Caddell, R.M., 2011. Metal Forming: Mechanics and Metallurgy. Cambridge University Press, New York, USA.
Jackson, P., Basinski, Z., 1967. Latent hardening and the flow stress in copper single crystals. Can. J. Phys. 45, 707–735.
Jahedi, M., Ardeljan, M., Beyerlein, I.J., Paydar, M.H., Knezevic, M., 2015a. Enhancement of orientation gradients during simple shear deformation by application of simple compression. J. Appl. Phys. 117, 214309.
Jahedi, M., Knezevic, M., Paydar, M., 2015b. High-Pressure double torsion as a Severe plastic deformation process: experimental procedure and finite element modeling. J. Mater. Eng. Perform. 24, 1471–1482.
Jahedi, M., Paydar, M.H., Zheng, S., Beyerlein, I.J., Knezevic, M., 2014. Texture evolution and enhanced grain refinement under high-pressure-double-torsion. Mater. Sci. Eng. A 611, 29–36.
Juul Jensen, D., Hansen, N., 1990. Flow stress anisotropy in aluminium. Acta Metall. Mater. 38, 1369–1380.
Kalidindi, S.R., Bronkhorst, C.A., Anand, L., 1992. Crystallographic texture evolution in bulk deformation processing of FCC metals. J. Mech. Phys. Solids 40, 537–569.
Khadyko, M., Dumoulin, S., Cailletaud, G., Hopperstad, O.S., 2016. Latent hardening and plastic anisotropy evolution in AA6060 aluminium alloy. Int. J. Plast. 76, 51–74.
Kitayama, K., Tomé, C.N., Rauch, E.F., Gracio, J.J., Barlat, F., 2013. A crystallographic dislocation model for describing hardening of polycrystals during strain path changes. Application to low carbon steels. Int. J. Plast. 46, 54–69.
Knezevic, M., Al-Harbi, H.F., Kalidindi, S.R., 2009. Crystal plasticity simulations using discrete Fourier transforms. Acta Mater. 57, 1777–1784.
Knezevic, M., Beyerlein, I.J., Brown, D.W., Sisneros, T.A., Tomé, C.N., 2013a. A polycrystal plasticity model for predicting mechanical response and texture evolution during strain-path changes: application to beryllium. Int. J. Plast. 49, 185–198.
Knezevic, M., Beyerlein, I.J., Lovato, M.L., Tomé, C.N., Richards, A.W., McCabe, R.J., 2014a. A strain-rate and temperature dependent constitutive model for BCC metals incorporating non-Schmid effects: application to tantalum–tungsten alloys. Int. J. Plast. 62, 93–104.
Knezevic, M., Capolungo, L., Tomé, C.N., Lebensohn, R.A., Alexander, D.J., Mihaila, B., McCabe, R.J., 2012. Anisotropic stress-strain response and microstructure evolution of textured α-uranium. Acta Mater. 60, 702–715.
Knezevic, M., Carpenter, J.S., Lovato, M.L., McCabe, R.J., 2014b. Deformation behavior of the cobalt-based superalloy Haynes 25: experimental characterization and crystal plasticity modeling. Acta Mater. 63, 162–168.
Knezevic, M., Crapps, J., Beyerlein, I.J., Coughlin, D.R., Clarke, K.D., McCabe, R.J., 2016a. Anisotropic modeling of structural components using embedded crystal plasticity constructive laws within finite elements. Int. J. Mech. Sci. 105, 227–238.
Knezevic, M., Kalidindi, S.R., Fullwood, D., 2008. Computationally efficient database and spectral interpolation for fully plastic Taylor-type crystal plasticity calculations of face-centered cubic polycrystals. Int. J. Plast. 24, 1264–1276.
Knezevic, M., Lebensohn, R.A., Cazacu, O., Revil-Baudard, B., Proust, G., Vogel, S.C., Nixon, M.E., 2013b. Modeling bending of α-titanium with embedded polycrystal plasticity in implicit finite elements. Mater. Sci. Eng. A 564, 116–126.
Knezevic, M., McCabe, R.J., Lebensohn, R.A., Tomé, C.N., Liu, C., Lovato, M.L., Mihaila, B., 2013c. Integration of self-consistent polycrystal plasticity with dislocation density based hardening laws within an implicit finite element framework: application to low-symmetry metals. J. Mech. Phys. Solids 61, 2034–2046.
Knezevic, M., McCabe, R.J., Tomé, C.N., Lebensohn, R.A., Chen, S.R., Cady, C.M., Gray Iii, G.T., Mihaila, B., 2013d. Modeling mechanical response and texture evolution of α-uranium as a function of strain rate and temperature using polycrystal plasticity. Int. J. Plast. 43, 70–84.
Knezevic, M., Zecevic, M., Beyerlein, I.J., Bingert, J.F., McCabe, R.J., 2015. Strain rate and temperature effects on the selection of primary and secondary slip and twinning systems in HCP Zr. Acta Mater. 88, 55–73.
Knezevic, M., Zecevic, M., Beyerlein, I.J., Lebensohn, R.A., 2016b. A numerical procedure enabling accurate descriptions of strain rate-sensitive flow of polycrystals within crystal visco-plasticity theory. Comput. Meth. Appl. Mech. Eng. 308, 468–482.
Knockaert, R., Chastel, Y., Massoni, E., 2000. Rate-independent crystalline and polycrystalline plasticity, application to FCC materials. Int. J. Plast. 16, 179–198.
Kocks, U.F., Brown, T.J., 1966. Latent hardening in aluminum. Acta Metall. 14, 87–98.
Kocks, U.F., Franciosi, P., Kawai, M., 1991. A forest model of latent hardening and its application to polycrystal deformations. Textures Microstruct. 14, 1103–1114.
Kocks, U.F., Mecking, H., 1981. Kinetics of flow and strain-hardening. Acta Metall. 29, 1865–1875.
Kubin, L., Devincre, B., Hoc, T., 2008a. Modeling dislocation storage rates and mean free paths in face-centered cubic crystals. Acta Mater. 56, 6040–6049.
Kubin, L., Devincre, B., Hoc, T., 2008b. Toward a physical model for strain hardening in fcc crystals. Mater. Sci. Eng. A 483, 19–24.
Lebensohn, R., 2001. N-site modeling of a 3D viscoplastic polycrystal using fast Fourier transform. Acta Mater. 49, 2723–2737.
Lebensohn, R., Solas, D., Canova, G., Brechet, Y., 1996. Modelling damage of Al-Zn-Mg alloys. Acta Mater. 44, 315–325.
Lebensohn, R.A., Tomé, C.N., 1993. A self-consistent anisotropic approach for the simulation of plastic deformation and texture development of polycrystals: application to zirconium alloys. Acta Metall. Mater. 41, 2611–2624.
Lebensohn, R.A., Turner, P.A., Signorelli, J.W., Canova, G.R., Tomé, C.N., 1998. Calculation of intergranular stresses based on a large-strain viscoplastic self-consistent polycrystal model. Model. Simulat. Mater. Sci. Eng. 6, 447.
Lebensohn, R.A., Zecevic, M., Knezevic, M., McCabe, R.J., 2016. Average intragranular misorientation trends in polycrystalline materials predicted by a viscoplastic self-consistent approach. Acta Mater. 104, 228–236.
Lentz, M., Klaus, M., Wagner, M., Fahrenson, C., Beyerlein, I.J., Zecevic, M., Reimers, W., Knezevic, M., 2015. Effect of age hardening on the deformation behavior of an Mg–Y–Nd alloy: in-situ X-ray diffraction and crystal plasticity modeling. Mater. Sci. Eng.,A 628, 396–409.
Lopes, A.B., Barlat, F., Gracio, J.J., Ferreira Duarte, J.F., Rauch, E.F., 2003. Effect of texture and microstructure on strain hardening anisotropy for aluminum deformed in uniaxial tension and simple shear. Int. J. Plast. 19, 1–22.
Lyttle, M.T., Wert, J.A., 1999. Precipitate-induced plastic anisotropy: explicit solutions of the plastic anisotropy due to plate-shaped precipitates. Metall. Mater. Trans. 30, 1283–1288.
Madec, R., Devincre, B., Kubin, L., Hoc, T., Rodney, D., 2003. The role of collinear interaction in dislocation-induced hardening. Science 301, 1879–1882.
Mánik, T., Holmedal, B., 2014. Review of the Taylor ambiguity and the relationship between rate-independent and rate-dependent full-constraints Taylor models. Int. J. Plast. 55, 152–181.
Masson, R., Bornert, M., Suquet, P., Zaoui, A., 2000. An affine formulation for the prediction of the effective properties of nonlinear composites and polycrystals. J. Mech. Phys. Solid. 48, 1203–1227.
Maudlin, P.J., Schiferl, S.K., 1996. Computational anisotropic plasticity for high-rate forming applications. Comput. Meth. Appl. Mech. Eng. 131, 1–30.
Merodio, J., Ogden, R.W., 2003. Instabilities and loss of ellipticity in fiber-reinforced compressible non-linearly elastic solids under plane deformation. Int. J. Solid Struct. 40, 4707–4727.
Meyers, M.A., Chawla, K.K., 2009. Mechanical Behavior of Materials, Cambridge.
Miao, W.F., Laughlin, D.E., 1999. Precipitation hardening in aluminum alloy 6022. Scripta Mater. 40, 873–878.
Needleman, A., 1988. Material rate dependence and mesh sensitivity in localization problems. Comput. Meth. Appl. Mech. Eng. 67, 69–85.
Neil, C.J., Wollmershauser, J.A., Clausen, B., Tomé, C.N., Agnew, S.R., 2010. Modeling lattice strain evolution at finite strains and experimental verification for copper and stainless steel using in situ neutron diffraction. Int. J. Plast. 26, 1772–1791.
Nguyen, G.D., 2005. A Thermodynamic Approach to Constitutive Modelling of Concrete Using Damage Mechanics and Plasticity Theory. University of Oxford.
Nugmanov, D., Knezevic, M., Zecevic, M., Sitdikov, O., Markushev, M., Beyerlein, I.J., 2018. Origin of plastic anisotropy in (ultra)-fine-grained Mg–Zn–Zr alloy processed by isothermal multi-step forging and rolling: experiments and modeling. Mater. Sci. Eng. A 713, 81–93.
Ortiz, M., Repetto, E.a, 1999. Nonconvex energy minimization and dislocation structures in ductile single crystals. J. Mech. Phys. Solid. 47, 397–462.
Pavlina, E., Lee, M.-G., Barlat, F., 2015. Observations on the nonlinear unloading behavior of advanced high strength steels. Metall. Mater. Trans. 46, 18–22.

Peirce, D., Asaro, R.J., Needleman, A., 1982. An analysis of nonuniform and localized deformation in ductile single crystals. Acta Metall. Mater. 30, 1087–1119.

Peirce, D., Asaro, R.J., Needleman, A., 1983. Material rate dependence and localized deformation in crystalline solids. Acta Metall. Mater. 31, 1951–1976.

Press, W.H., Teukolsky, S.A., Vetterling, W.T., Flannery, B.P., 1992. Numerical Recipes in Fortran 77, second ed. Cambridge University Press.

Rauch, E.F., Gracio, J.J., Barlat, F., 2007. Work-hardening model for polycrystalline metals under strain reversal at large strains. Acta Mater. 55, 2939–2948.

Rauch, E.F., Gracio, J.J., Barlat, F., Lopes, A.B., Ferreira Duarte, J., 2002. Hardening behavior and structural evolution upon strain reversal of aluminum alloys. Scr. Mater 46, 881–886.

Risse, M., Lentz, M., Fahrenson, C., Reimers, W., Knezevic, M., Beyerlein, I.J., 2017. Elevated temperature effects on the plastic anisotropy of an Extruded Mg-4 Wt Pct Li alloy: experiments and polycrystal modeling. Metall. Mater. Trans. 48, 446–458.

Savage, D.J., Knezevic, M., 2015. Computer implementations of iterative and non-iterative crystal plasticity solvers on high performance graphics hardware. Comput. Mech. 56, 677–690.

Schmid, E., Boas, W., 1950. Plasticity of Crystals with Special Reference to Metals. English translation F.A. Hughes, London.

Schröder, J., Miehe, C., 1997. Aspects of computational rate-independent crystal plasticity. Comput. Mater. Sci. 9, 168–176.

Sehitoglu, H., Foglesong, T., Maier, H.J., 2005. Precipitate effects on the mechanical behavior of aluminum copper alloys: Part II. Modeling. Metall. Mater. Trans. 36, 763–770.

Shaffer, J.B., Knezevic, M., Kalidindi, S.R., 2010. Building texture evolution networks for deformation processing of polycrystalline fcc metals using spectral approaches: applications to process design for targeted performance. Int. J. Plast. 26, 1183–1194.

Simo, J.C., Taylor, R.L., 1985. Consistent tangent operators for rate-independent elastoplasticity. Comput. Meth. Appl. Mech. Eng. 48, 101–118.

Tabourot, L., Fivel, M., Rauch, E., 1997. Generalised constitutive laws for fcc single crystals. Mater. Sci. Eng. A 234, 639–642.

Taylor, G.I., 1938. Plastic strain in metals. J. Inst. Met. 62, 307–324.

Taylor, G.I., Elam, C.F., 1923. Bakerian lecture. the distortion of an aluminium crystal during a tensile test. Proc. Roy. Soc. Lond.: Mathematical, Physical and Engineering Sciences. The Royal Society 643–667.

Teodosiu, C., Raphanel, J.L., 1991. Finite element simulations of large elastoplastic deformations of multicrystals. Proceedings of the International Seminar MECAMAT91 153–168.

Tian, H., Brownell, B., Baral, M., Korkolis, Y.P., 2016. Earing in cup-drawing of anisotropic Al-6022-T4 sheets. Int. J. Material Form. 1–15.

Turner, P.A., Tomé, C.N., 1994. A study of residual stresses in Zircaloy-2 with rod texture. Acta Metall. Mater. 42, 4143–4153.

Wagoner, R.H., Lim, H., Lee, M.-G., 2013. Advanced issues in springback. Int. J. Plast. 45, 3–20.

Wen, W., Borodachenkova, M., Tomé, C.N., Vincze, G., Rauch, E.F., Barlat, F., Grácio, J.J., 2015. Mechanical behavior of Mg subjected to strain path changes: experiments and modeling. Int. J. Plast. 73, 171–183.

Wollmershauser, J.A., Clausen, B., Agnew, S.R., 2012. A slip system-based kinematic hardening model application to in situ neutron diffraction of cyclic deformation of austenitic stainless steel. Int. J. Fatigue 36, 181–193.

Wu, T.-Y., Bassani, J.L., Laird, C., 1991a. Latent hardening in single crystals I. Theory and experiments. Proc. Math. Phys. Sci. 435, 1–19.

Wu, T.-Y., Bassani, J.L., Laird, C., 1991b. Latent hardening in single crystals I. Theory and experiments. Proc. Roy. Soc. Lond.: Mathematical, Physical and Engineering Sciences 435, 1–19.

Yoon, J.W., Barlat, F., Gracio, J.J., Rauch, E., 2005. Anisotropic strain hardening behavior in simple shear for cube textured aluminum alloy sheets. Int. J. Plast. 21, 2426–2447.

Yoshida, K., Brenner, R., Bacroix, B., Bouvier, S., 2009. Effect of regularization of Schmid law on self-consistent estimates for rate-independent plasticity of polycrystals. Eur. J. Mech. Solid. 28, 905–915.

Yoshida, K., Kuroda, M., 2012. Comparison of bifurcation and imperfection analyses of localized necking in rate-independent polycrystalline sheets. Int. J. Solid Struct. 49, 2073–2084.

Zecevic, M., Beyerlein, I.J., Knezevic, M., 2017a. Coupling elasto-plastic self-consistent crystal plasticity and implicit finite elements: applications to compression, cyclic tension-compression, and bending to large strains. Int. J. Plast. 93, 187–211.

Zecevic, M., Knezevic, M., 2015. A dislocation density based elasto-plastic self-consistent model for the prediction of cyclic deformation: application to AA6022-T4. Int. J. Plast. 72, 200–217.

Zecevic, M., Knezevic, M., Beyerlein, I.J., Tomé, C.N., 2015a. An elasto-plastic self-consistent model with hardening based on dislocation density, twinning and detwinning: application to strain path changes in HCP metals. Materials Science and Engineering: A 638, 262–274.

Zecevic, M., Korkolis, Y.P., Kuwabara, T., Knezevic, M., 2016a. Dual-phase steel sheets under cyclic tension–compression to large strains: experiments and crystal plasticity modeling. J. Mech. Phys. Solids 96, 65–87.

Zecevic, M., McCabe, R.J., Knezevic, M., 2015b. A new implementation of the spectral crystal plasticity framework in implicit finite elements. Mech. Mater. 84, 114–126.

Zecevic, M., McCabe, R.J., Knezevic, M., 2015c. Spectral database solutions to elasto-viscoplasticity within finite elements: application to a cobalt-based FCC superalloy. Int. J. Plast. 70, 151–165.

Zecevic, M., Pantleon, W., Lebensohn, R.A., McCabe, R.J., Knezevic, M., 2017b. Predicting intragranular misorientation distributions in polycrystalline metals using the viscoplastic self-consistent formulation. Acta Mater. 140, 398–410.

Zecevic, M., Roemer, T., Knezevic, M., Korkolis, Y., Kinsey, B., 2016b. Residual ductility and microstructural evolution in Continuous-bending-under-tension of AA-6022-T4. Materials 9, 130.

Zhang, K., Holmedal, B., Hopperstad, O.S., Dumoulin, S., Gawad, J., Van Bael, A., Van Houtte, P., 2015. Multi-level modelling of mechanical anisotropy of commercial pure aluminium plate: crystal plasticity models, advanced yield functions and parameter identification. Int. J. Plast. 66, 3–30.